Permeability of Intact and Fractured Cobourg Limestone

By

Chong CAO

Department of Civil Engineering and Applied Mechanics

McGill University, Montreal

December 2016

A thesis submitted to

McGill University

in partial fulfillment of the requirements of the degree of

Master of Engineering

ABSTRACT

This study deals with the application of a transient hydraulic pulse technique to measure the permeability characteristics of intact Cobourg Limestone cubes. The proposed method makes use of a specially designed pressurization system to generate hydraulic pulses within a sealed cavity. The cavity pressure is then allowed to dissipate as the fluid migrates into the saturated rock. Crucial to interpreting permeability from transient test is the influence of entrapped air bubbles within the pressurized cavity. The modelling results indicate that the air inclusions can significantly increase the compressibility of the fluid in the pressurized cavity, leading to a delay in the decay of the hydraulic pulse, which may cause underestimation of rock permeability.

Normal fractures are created by performing tensile splitting of cuboidal samples. Steady-state radial flow tests are utilized to measure the permeability of fracture under compression. The permeability of fracture is found to be significantly higher than that of the intact rock matrix. Experimental results show that fracture permeability can be reduced by up to four orders of magnitude as the normal stress acting on the fracture is increased. Special attention has been given to the hysteresis behavior of fracture permeability under repeated loading-unloading cycles.

RÉSUMÉ

Cette étude applique test de impulsion transitoire pour mesurer les caractéristiques de faible perméabilité de cubes intactes de Cobourg calcaire. La méthode proposée utilise un système de pressurisation spécialement conçu pour générer des impulsions hydrauliques dans la cavité scellée. La pression de la cavité est alors autorisé à se dissiper que le fluide migre dans la matrice rocheuse saturée. Cruciale pour interpréter la perméabilité transitoire de ce test de perméabilité à la surface est l'influence des bulles d'air piégées à l'intérieur de la cavité sous pression. Les résultats de la modélisation indiquent que les inclusions d'air peuvent augmenter de manière significative la compressibilité du fluide et donc retarder le processus d'impulsion de diminution hydraulique, qui peut conduire à une sous-estimation de la perméabilité de la roche.

Fractures normales sont créées en effectuant un essai de traction de fendage. Les essais d'écoulement radial à l'état d'équilibre sont utilisés pour mesurer la perméabilité de fracture en compression. La perméabilité de fracture se trouve être significativement plus élevé que la rocheuse intacte. Les résultats expérimentaux montrent que la perméabilité à la fracture peut être alterné par trois échelles de grandeur sous différents niveaux de contrainte de la compression. Un point particulière a été apporté au comportement d'hystérésis de perméabilité de fracture dans des cycles répétés de chargement-déchargement.

ACKNOWLEDGEMENT

I would like to express my sincere gratitude to my supervisor Professor A.P.S. Selvadurai, the William Scott Professor and James McGill Professor of the Department of Civil Engineering and Applied Mechanics, for his guidance through my thesis research at McGill University. His scientific knowledge and exquisite insight quickly introduced me to the frontier of the research field.

Special thanks are expressed to Mr. John Bartczak, technician of the Civil Engineering Department at McGill University, for his technical assistance through my research work. He spent much time discussing with me in detail about my experiments, from experiment design to sample preparation.

I would also like to give my sincere appreciation to my colleagues in Environmental Geomechanics Laboratory for their help and discussion about my experiments during the last two years.

Finally, I would like to give my sincere appreciation to my parents and my sister. Their support is the biggest source of my motivation.

TABLE OF CONTENTS

LIST OF FIGURES

LIST OF TABLES

CHAPTER 1
INTRODUCTION

Worldwide efforts have been directed to investigating the feasibility of constructing Deep Geological Repositories (DGR) for the disposal of radioactive nuclear waste. The low permeable host rock and the great depth would ideally ensure an isolated environment for the hazardous materials over 10^6 years. Comprehensive studies at the Äspö Hard Rock Laboratory in Sweden (e.g., Thörn *et al.*, 2015), the Yucca Mountain site in USA (e.g., Bodvarsson *et al.*, 1999), the Grimsel rock laboratory in Switzerland (e.g., Alonso *et al.*, 2005), the Bure site in France (e.g., Delay *et al.*, 2007), the Beishan area in China (e.g., Chen *et al.*, 2014), and the Underground Research Laboratory in Canada (e.g., Souley *et al.*, 2001) have provided insights into the fundamental processes influencing groundwater flow and radioactive substances transport in geological formations.

Argillaceous formations of sufficient thickness, with low permeability and high sorption capacity, have been investigated by Canadian nuclear waste management agencies as potential host rocks for the long-term storage of low- and intermediate- level nuclear waste (Jensen *et al.*, 2007). The proposed DGR mainly involves a series of waste emplacement rooms that are excavated at a depth of 680 m beneath Bruce Nuclear site, Ontario (Figure 1.1). The *in situ*

permeability of the Ordovician age argillaceous formations of Cobourg Limestone has been measured to be between 10^{-22} and 10^{-20} m^2. The extremely low permeability characteristics favors Cobourg Limestone as an effective barrier to radionuclide migration.

Although intact rock masses are desirable as repository rocks for geological disposal, such formations are rare. Most sites will contain sparsely located fractures, as shown in Figure 1.2. The presence of natural fractures/joints within rock masses can significantly alter the mechanical behavior and lead to an increase in the hydraulic conductivity of geological formations. The ability of fractured geological formations to transport fluid and contaminants is mainly controlled by the geometry of the fracture system and *in situ* stress state. The existing stress field can be altered by thermal loading (e.g., heat from radioactive decay of the waste), construction activities (e.g., underground excavations and groundwater lowering) and natural geological processes (e.g., earthquakes and glaciation). The stress field perturbations may alter the normal and shear stresses acting across fracture planes and change the fracture permeability. Therefore, hydro-mechanical coupling in porous media containing isolated or sparse fractures is an important issue for developing strategies for the underground storage of nuclear waste (Selvadurai and Nguyen, 1997; Rutqvist and Stephansson, 2003).

Numerous laboratory-scale experimental studies have been conducted in efforts to understand fracture permeability evolution under variable loading conditions. The normal stress-dependent permeability properties of fractures have been investigated by conducting either radial or rectilinear flow tests on a single fracture (Raven and Gale, 1985; Iwano, 1995). Experimental results show that hydro-mechanical coupling exhibits hysteresis characteristics during loading-

unloading cycles. For example, fracture permeability in granite samples measuring 450 mm in diameter can be altered by up to three orders of magnitude under different levels of compressive stress up to 8 MPa (Selvadurai, 2015). The experimental techniques for the application of shear stress to rock samples include direct shear tests on nominally horizontal fractures, rotary shear tests on hollow cylindrical fractures, and sliding tests on inclined fractures (Esaki et al., 1999; Lee and Cho, 2002; Hans and Boulon, 2003; Olsson and Brown, 1993; Teufel, 1987; Nemoto *et al.*, 2008; Jing and Stephansson, 1995). Fracture surface roughness causes dilation during shear as well as asperity degradation during the application of combined normal stress and shear displacement. Gouge production tends to be the dominant factor influencing fracture permeability under high normal stresses, since gouge materials can impede fluid flow through fractures.

Fluid flow within rough-walled fractures can be numerically described by either the Navier-Stokes equations, or in simplified forms by Stokes' equations and the equation for the theory of lubrication developed by Reynolds (Zimmerman and Yeo, 2000; Yeo *et al.*, 1998; Watanabe *et al.*, 2008). Fracture surface roughness can be incorporated into numerical models for simulation of hydro-mechanical coupling. Shear dilation and channeling effects are responsible for anisotropic flow through a single fracture. Computational simulations have also been conducted on rock masses containing random fractures with stress-dependent aperture alterations (Min *et al.*, 2004; Zhou *et al.*, 2008; Latham *et al.*, 2013). The block-scale permeability is dependent on both the loading condition and fracture orientation (Figure 1.3). The influences of fracture surface degradation and gouge production on fracture permeability have been implemented into rock joint models (Boulon *et al.*, 1993; Nguyen and Selvadurai,

1998). In all the computational approaches discussed above, the load-fracture closure and stress-permeability properties of a single fracture are the key input parameters.

The objective of this thesis is to experimentally measure the permeability characteristics of intact and fractured Cobourg Limestone. Radial flow hydraulic pulse tests will be conducted on intact rock samples. The finite element approach developed by Selvadurai and Najari (2015) is capable of simulating the transient diffusion of pore water pressure through the saturated rock matrix as well as considering the influences of trapped air bubbles within the pressurized cavity. In this research, the procedure is applied to an axisymmetric radial flow configuration similar to that used by Selvadurai and Carnaffan (1997), Selvadurai and Jenner (2013) and Selvadurai and Najari (2016) to examine the Cobourg Limestone. In order to study the fracture permeability evolution under compressive stresses, steady-state radial flow tests will be performed on cuboidal samples with normal fractures. Special attention will be given to the hysteresis behavior of fracture permeability during loading and unloading cycles.

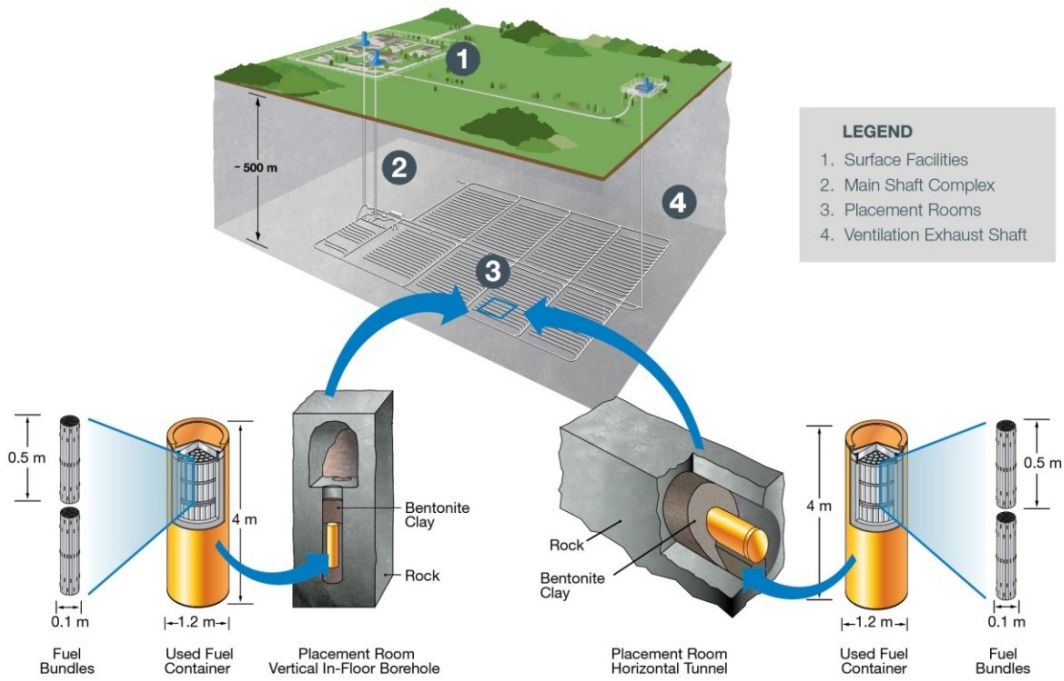

Figure 1.1 Project description of the proposed Deep Geological Repository

(Nuclear Waste Management Organization, 2011)

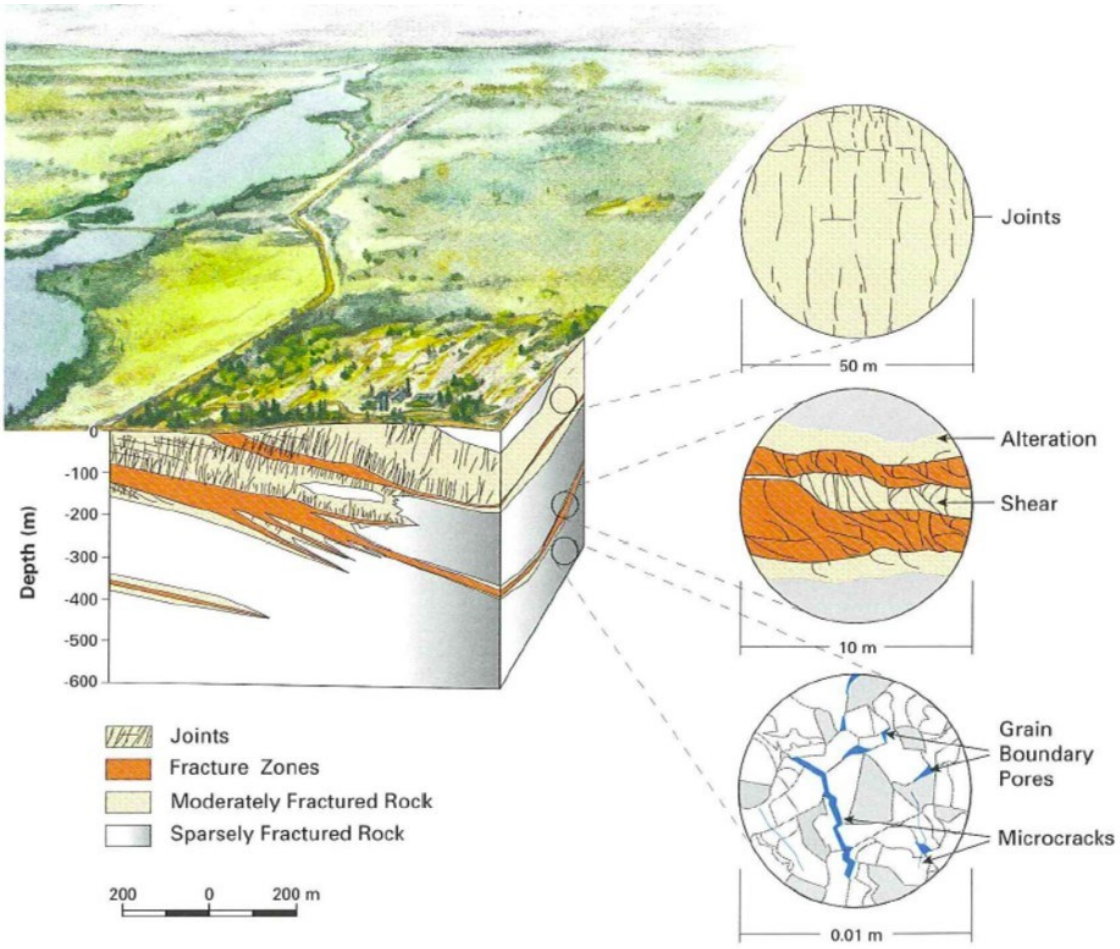

Figure 1.2 Fractures in geological formations

(Atomic Energy of Canada Ltd., 1994)

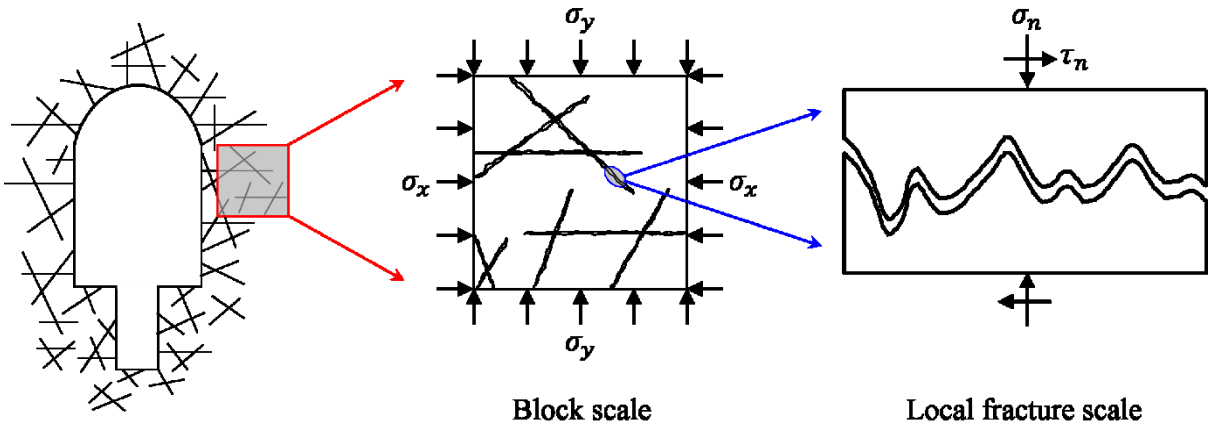

Figure 1.3 2-D computational modelling scheme for fractured porous medium

CHAPTER 2
LITERATURE REVIEW

Permeability is an important parameter that can influence geo-environmental problems dealing with groundwater contamination, deep geological disposal of radioactive nuclear wastes, oil/gas production in petroleum reservoirs, geological sequestration of carbon dioxide, etc. Considerable laboratory efforts have been devoted to measuring the transport properties of low permeability geomaterials under different mechanical and environmental conditions.

2.1 Intact Permeability

Steady-state flow tests are commonly employed to measure the permeability of porous materials, using either liquid (e.g., water and ethanol) or gas (e.g., nitrogen, argon, and helium) as the permeating fluid. Darcy's flow is established by applying constant pressure gradient in axial/radial direction. The flow rate can be measured by recording the flow rate from high-precision pumps and weighing the collected outflow with either a scale or gas flow meter. The time required to reach equilibrium state can range from several minutes to a few weeks depending on the material permeability and sample size.

Transient pulse tests have been widely used to estimate the transport properties of low-permeability geomaterials ($K < 10^{-18}$ m^2). This technique mainly involves the instantaneous pressurization of a fluid volume that is in direct contact with the deformable porous medium and allowing the pore pressure to diffuse through the permeable rock matrix. The decay pattern of the pressure within the fluid-filled pressurization system can be monitored and quantitatively related to the permeability of the rock. The transient test overcomes the difficulties of applying extremely low flow rates and long duration tests that are required for performing steady-state test on tight rocks.

Published permeability values for typically low-permeability rocks are summarized in Table 2.1. The pore fluid pressure or transient pulses range from 100 kPa to 40 MPa for these tests. Sealing effectiveness poses a crucial challenge for accurately measuring low permeabilities, since unexpected pressure leakage always occurs at connections and interfaces. The rock permeability tends to be overestimated when the sealing leakage is significant enough to alter the steady-state or transient response of the pressurization system. Typical sealing techniques include rubber membrane seal in high pressure tri-axial cell and epoxy coating on interfaces.

2.2 Fracture Permeability

Rock fractures/joints may exhibit highly nonlinear mechanical behavior during normal loading and unloading processes. The existing models for aperture closure proposed for rock fractures under compressive loading conditions are summarized in Table 2.2. The presence of roughness on the fracture surface can cause hysteresis in the compression-closure behavior as well as

energy dissipation due to frictional slip (Selvadurai and Yu, 2005). The hydraulic aperture differs from the mechanical aperture depending on the geometric parameters of the fracture, which may include asperity distribution, asperity contact area and tortuosity. In order to numerically describe the hydraulic permeability of rock discontinuities, empirical models have been proposed for the relationship between hydraulic aperture and mechanical aperture, as listed in Table 2.3.

Fracture dilation during shear and gouge production due to fracture degradation are the two competing factors that can influence the permeability of a fracture under combined normal and shear loading (Figure 2.1). Sliding-induced shear dilation enlarges fracture apertures and significantly increases rock permeability, while the degradation of contacting asperities may produce gouge particles and block pathways for fluid transport. Normal stresses tend to reduce fracture permeability by either inhibiting shear dilation or enhancing gouge production. The published results of shear loading experiments are summarized in Table 2.4. Despite numerous studies undertaken, the effects of asperity breakage and gouge production on fracture permeability evolution have not been extensively studied experimentally. This is not only due to the irregular nature and complex three-dimensional topography of rock fractures, but is also the result of inadequate shear flow devices and inaccurate permeability measuring techniques.

Gouge materials have been observed in deep fault zones and are generally considered to be an important factor influencing frictional sliding and permeability evolution of natural faults (Morrow *et al*., 1984). Laboratory-scale shearing tests suggest that gouge formation results from the successive degradation of contacting asperities across a rough-walled fracture.

Coarse-grained gouge particles can undergo compaction and grain crushing during shear sliding, and consequently fine-grained gouge materials tend to reduce fault permeability. In contrast, dilatancy of granular gouges may facilitate fluid flow through gouge-filled natural faults. Although gouge production within fault zones is critical to the performance assessment of a DGR, the hydro-mechanical properties of gouge-filled fractures have not been explicitly incorporated into existing numerical models.

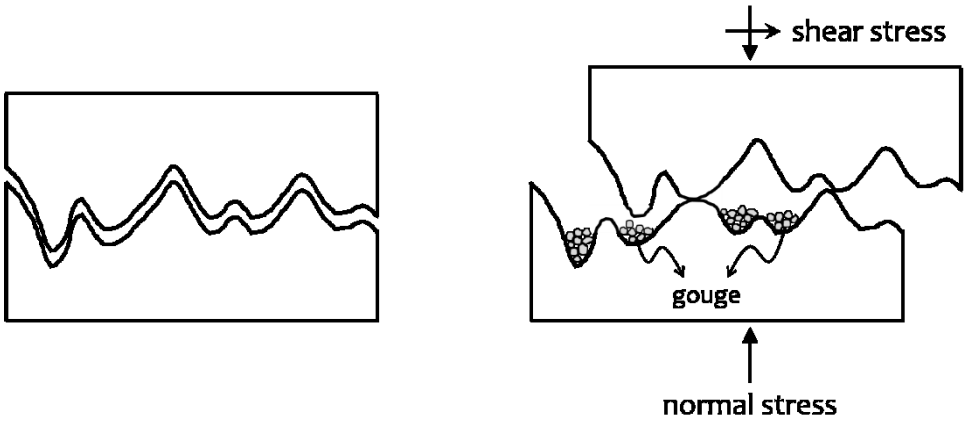

Figure 2.1 Shear dilation and gouge production

Table 2.1 Selected permeability tests on tight rocks

Research	Material	Testing method	Permeating fluid	Sample	Permeability K (m^2)
Brace et al. (1968)	Granite	Transient	Water/Argon	Cylinder	10^{-21} – 10^{-19}
Bernaix (1969)	Gneiss	Steady-state	Water	Hollow cylinder	10^{-21} – 10^{-18}
Neuzil et al. (1981)	Shale	Transient	Water	Cylinder	10^{-19} – 10^{-17}
Bernabé et al. (1986)	Granite	Transient	Water	Cylinder	10^{-21} – 10^{-18}
Escoffier et al. (2005)	Mudstone	Transient	Water	Cylinder	10^{-21} – 10^{-20}
Selvadurai & Jenner (2013)	Limestone	Transient	Water	Hollow cylinder	10^{-22} – 10^{-19}
Selvadurai & Najari (2016)	Limestone	Steady-state	Water	Hollow cylinder	10^{-20} – 10^{-19}
Chen et al. (2014)	Granite	Transient	Nitrogen gas	Cylinder	10^{-20} – 10^{-19}
Pan et al. (2015)	Shale	Transient	Helium gas	Cube	10^{-21} – 10^{-19}
Li et al. (2016)	Shale	Steady-state	Methane gas	Cube	10^{-19} – 10^{-17}

Table 2.2 Constitutive models proposed for fracture under normal loading

Research	Constitutive model	Symbols
Goodman (1976)	$\delta = A + B\ln\sigma$	δ : normal closure
Bandis et al. (1983)	$\delta = \dfrac{\sigma}{k_{ni} + \sigma/\delta_{\max}}$	σ : normal stress $\delta_{\max}$: maximum closure
Rutqvist et al. (2002)	$\delta = \delta_{\max}\left[1 - \exp(-\alpha\sigma)\right]$	k_{ni} : initial normal stiffness
Xie et al. (2014)	$\delta = \delta_{\max}\left\lvert 1 - \dfrac{1}{\ln(\sigma/k_{ni} + 1) + 1}\right\rvert$	A, B, α : constants

Table 2.3 Hydraulic fracture aperture vs Mechanical fracture aperture

Research	Proposed model	Symbols
Witherspoon et al. (1979)	$e_h = e_{h0} + f\Delta e_m$	e_h: hydraulic aperture e_{h0}: initial hydraulic aperture e_m: mechanical aperture Δe_m: mechanical aperture change JRC: joint roughness coefficient f: constant
Barton et al. (1985)	$e_h = \dfrac{e_m^2}{JRC^{2.5}}$	

Table 2.4 Selected flow tests on rock fractures subjected to shear

Fracture Orientation	Research	Normal Stress (MPa)	Shear (mm)	Gouge Production	Permeability K (m^2)
Normal Fracture	Olsson & Brown (1993)	4.3	0 – 3.5	Yes	10^{-11} – 10^{-9}
	Yeo et al. (1998)	0	0 – 2	No	10^{-8} – 10^{-7}
	Esaki et al. (1999)	1 – 20	0 – 20	Yes	10^{-10} – 10^{-8}
	Lee & Cho (2002)	1 – 3	0 – 15	Yes	10^{-11} – 10^{-8}
	Hans & Boulon (2003)	2 – 10	0 – 10	No	10^{-11} – 10^{-10}
	Watanabe et al. (2008)	10 – 100	0 – 10	No	10^{-13} – 10^{-9}
Inclined Fracture	Morrow et al. (1984)	5 – 200	0 – 10	Yes	10^{-22} – 10^{-18}
	Teufel (1987)	0 – 130	0 – 7	Yes	10^{-17} – 10^{-13}
	Nemoto et al. (2008)	0 – 50	0 – 12	Yes	10^{-12} – 10^{-9}

CHAPTER 3
THE COBOURG LIMESTONE

The argillaceous Cobourg Limestone is being considered as a suitable host rock for the long-term storage of low- and intermediate- level nuclear waste (NWMO, 2011). The selected limestone formation is seismically quiet and geomechanically stable. The low permeability of the Cobourg Limestone and the great depth of the repository location create an isolated environment for the storage of the hazardous material. Multiple low permeability bedrock formations ensure that the contaminant transport will be diffusion dominated. These favorable geological features enable Cobourg Limestone formation as an ideal geological setting for the proposed DGR.

3.1 Regional Geosynthesis

An 840 m thick sedimentary sequence of Cambrian to Devonian age near horizontally bedded, weakly deformed shales, carbonates and evaporites of the Michigan Basin is situated beneath the Bruce site, located at 225 km northwest of Toronto on the eastern shore of Lake Huron. Within this sedimentary setting, the proposed DGR would be excavated inside the low

permeability Ordovician limestone Cobourg (Lindsay) Formation at a depth of 680 m, which is sandwiched between 200 m of upper shale formations and 150 m of lower carbonate formations. The geological cross-section through the Michigan Basin is illustrated in Figure 3.1 and the stratigraphy beneath the Bruce nuclear site is schematically shown in Figure 3.2.

Multiple low permeability bedrock formations (10^{-23} m^2 to 10^{-19} m^2), acting as natural barriers, enclose and overlie the proposed DGR (Figure 3.3). Hydraulic measurements show that no transmissive vertical or subvertical faulting exists in the deep or intermediate groundwater regimes. Geochemical evidence points to the high salinity of the ancient deep groundwater at the proposed repository depth, indicating geological isolation for a long period without glacial perturbation or cross-formational flow. Therefore, the contaminant transport through the geological formations hosting the proposed DGR is considered to be diffusion dominated.

Construction experience with the excavation of deep underground openings in the Cobourg Formation indicates that excavated openings in either the Ordovician shale or Ordovician limestone could be dry and stable. The planned DGR is located in a seismically quiet portion of the craton, which is comparable to the stable Canadian Shield setting. No evidence has been found for the presence of structural features that would indicate a high seismic hazard near the Bruce nuclear site.

3.2 Material Properties

The Cobourg Limestone mainly contains two distinct compositions: the lighter carbonate

nodular rock and the darker argillaceous material (Figure 3.4). The argillaceous partings in a quartzitic rock give the Cobourg Limestone a nominally stratified appearance. Major mineralogical components of the rock include 81 % of calcite, 8 % of dolomite, 3 % of quartz, and 6 % of sheet silicates (NWMO, 2011).

Experiments have been conducted by Letendre (2010), Jenner (2011) and Hekimi (2012) to examine the physical and chemical properties of intact Cobourg Limestone. The mechanical properties for Cobourg Limestone are summarized in Table 3.1.

3.3 Sample Preparation

Blocks of the Cobourg Limestone were obtained from the Saint Mary's quarry in Bowmanville, ON. The sample contains some sparsely located fractures, which should be avoided during cutting in order to obtain intact cubes. Large blocks were cut into smaller cubes (150 mm, 250 mm, and 350 mm). The cuboidal surfaces were machined to a smooth finish on a lathe. In this study, three 150-mm cubes have been utilized for investigating the permeability of Cobourg Limestone.

A 20-mm diameter cylindrical cavity that can be utilized for fluid injection during permeability testing was cored half-way through the cuboidal sample (Figure 3.5). The chosen sample was cored with its axis perpendicular to the nominal bedding plane and thus the stratification was considered to be nominally horizontal (Figure 3.6). The geometric configuration of both intact and fractured Cobourg Limestone sample is illustrated in Figure 3.7 and the geometric

properties for each sample are listed in Table 3.2.

The upper surface of the rock sample was attached to stainless steel plate using Marine epoxy supplied by LePage^{TM}. The sealing techniques are shown in Figure 3.8. The steel plate contains one threaded cavity, which can be connected to the pressurization system through a stainless steel nipple. The extra epoxy blocking the central cavity were carefully drilled and cleaned around threads.

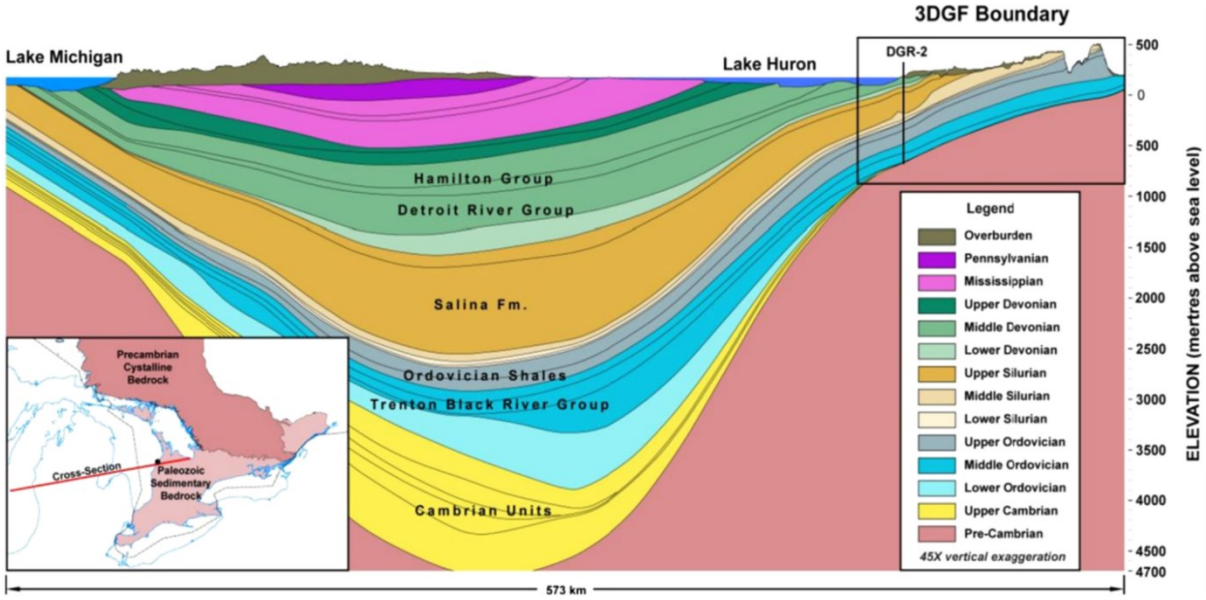

Figure 3.1 Geological cross-section through the Michigan Basin

(Nuclear Waste Management Organization, 2011)

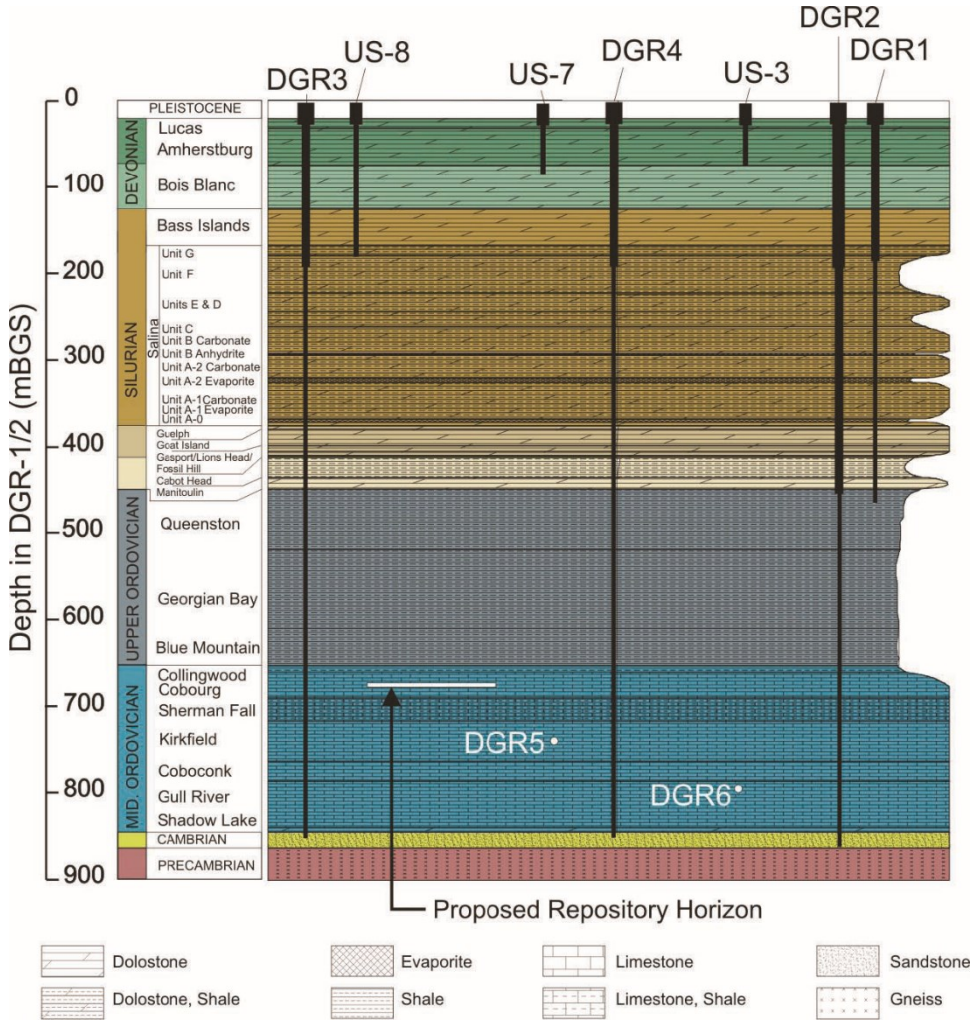

Figure 3.2 Subsurface stratigraphy at the Bruce nuclear site

(Nuclear Waste Management Organization, 2011)

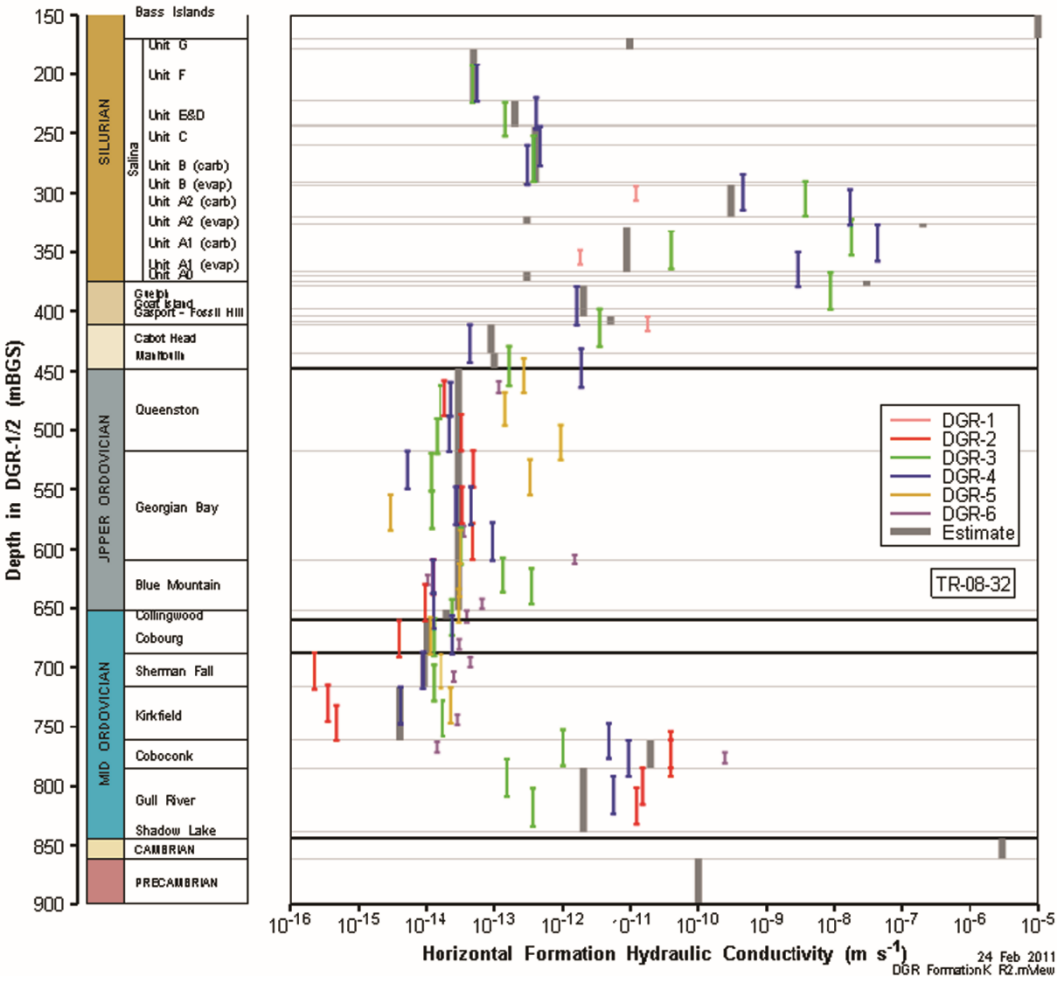

Figure 3.3 Horizontal hydraulic conductivities estimated from borehole tests

(Nuclear Waste Management Organization, 2011)

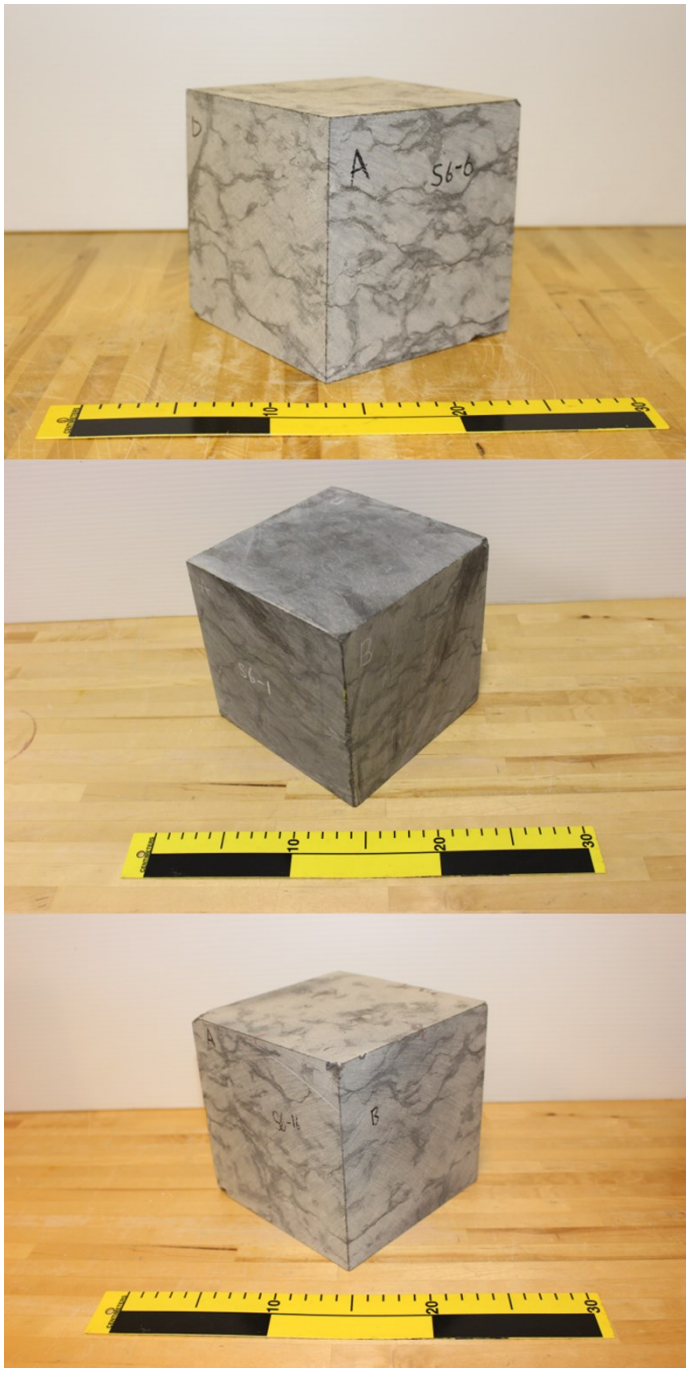

Figure 3.4 Photographs of Cobourg Limestone samples

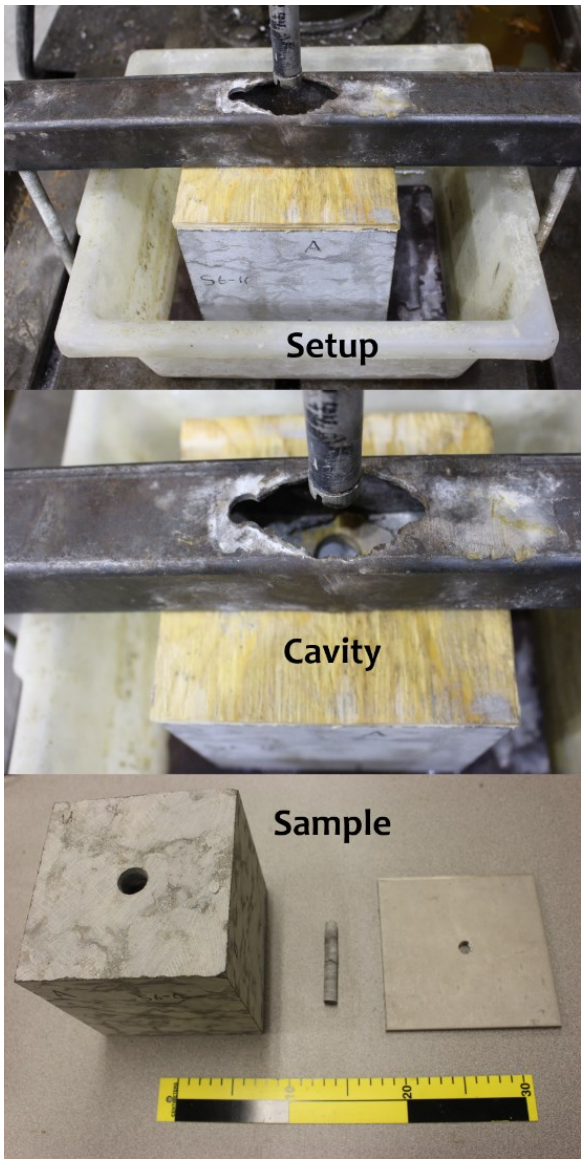

Figure 3.5 Coring

Figure 3.6 Extended view of Cobourg Limestone cubes showing stratification

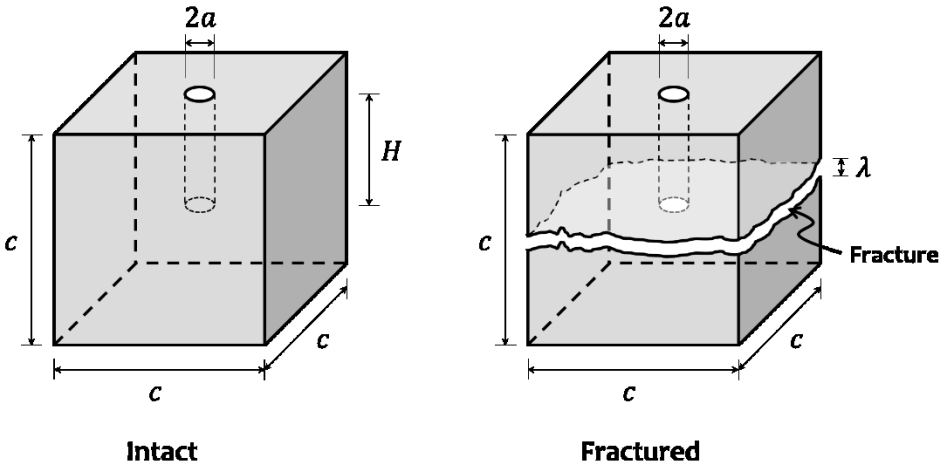

Figure 3.7 Geometric configuration of Cobourg Limestone cubes

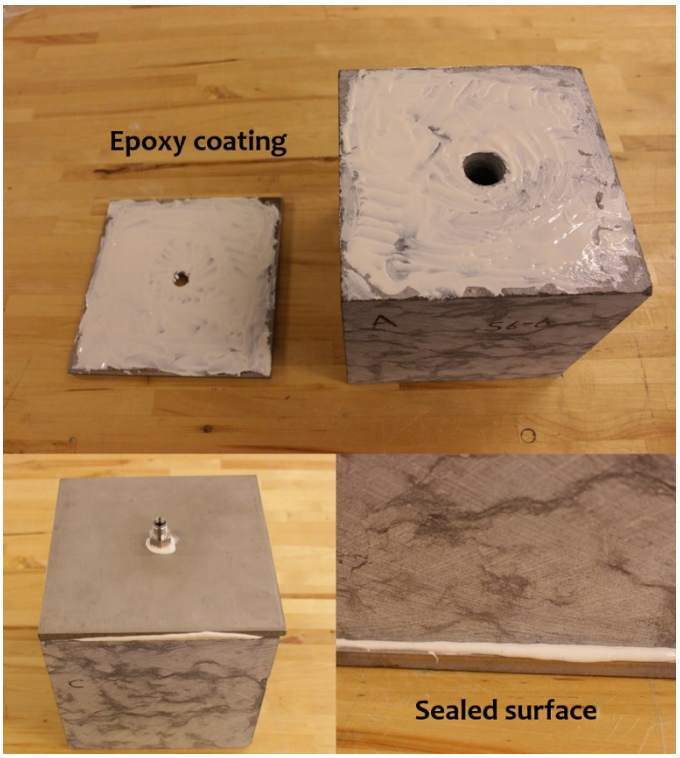

Figure 3.8 Marine epoxy sealing

Table 3.1 Mechanical properties for Cobourg Limestone

Properties	Values
Compressive strength (σ)	91.4 MPa
Splitting tensile strength (σ_t)	6.8 MPa
Elastic modulus (E)	20.8 GPa
Poisson's ratio (v)	0.25
Compressibility ($C_{eff} = 3(1-2v)/E$)	7.211×10^{-11} m^2/N
Porosity (n)	1%
Density (ρ)	2680 kg/m^3

Table 3.2 Geometric properties for cuboidal samples

Properties	Sample Characteristic		
	S6-6	S6-11	S6-16
Sample dimensions $c\times c\times c$ (mm^3)	152.7×150.9×152.5	152.4×154.8×150.6	152.9×151.2×151.1
Central cavity $2a$ (mm)	20.9	20.5	20.6
Cavity height H (mm)	79.9	84.1	86.3
Equivalent fluid column H_w (mm)	107.8	119.1	118.9

CHAPTER 4
INTACT PERMEABILITY

In previous studies, the *in situ* permeability of Cobourg Limestone geological formations has been measured to be between 10^{-22} and 10^{-20} m^2 (NWMO, 2011). This study applies hydraulic pulse tests to measure intact permeability of Cobourg Limestone in order to confirm its suitability for the long-term storage of the nuclear waste. The transient test results are further verified by pressure-controlled steady-state tests.

4.1 Hydraulic Pulse Tests

Hydraulic pulse tests have been widely used to estimate the fluid transport properties of low-permeability geomaterials ($K < 10^{-18}$ m^2). The proposed study will use radial flow hydraulic pulse test to measure the permeability of intact Cobourg Limestone. This technique involves the instantaneous pressurization of a fluid volume within the rock cavity and allowing the cavity pressure to dissipate as the fluid migrates into the saturated permeable rock matrix. The decay pattern of the pressure within the fluid-filled cavity can be monitored and used to calculate the permeability of the rock. The transient test overcomes the difficulties of applying

extremely low flow rates and continuing painfully long time that are required for performing steady-state test on tight rocks.

4.1.1 Experimental configuration

The pressurization system (Figure 4.1) includes a cross that has been connected to the sample cavity, a pressure transducer, a connection containing a de-airing pipe and water inlet. The water inlet pipe measures 3 mm (1/8 in) in diameter and occupies the entire length of the central cavity. This special set-up ensures that water flow into the cavity bottom and flush out any residual air bubbles through the top de-airing pipe. All connections to the pressurizing system are sealed with Marine epoxy in order to eliminate pressure leakage.

A cylindrical Venturi vacuum pump (Vaccon JS-150M-STAA4 generating up to 28 inches of Hg and 3.5 SCFM of vacuum flow) is connected to the de-airing valve for the purpose of completely removing residual air bubbles from the cavity through vacuum suction (Figure 4.2). Vacuum condition is produced by forcing compressed air through a nozzle. As the air exits the nozzle, it expands in volume and increases in velocity to supersonic speed before entering the diffuser. This creates a constant vacuum flow at the suction port, which is located between the nozzle and diffuser. The trapped air bubbles can therefore be extracted through the de-airing pipe.

The vacuum chamber is utilized to saturate the rock sample with de-aired water (Fig. 4.3). Another cylindrical Venturi vacuum pump is connected to the sealed stainless steel container, which contains de-aired water. Sealing has been provided by the rubber O-ring. The vacuum

condition is produced at 26.5 inches of Hg, which can be interpreted as -90 kPa. The dry sample is immersed under water in the vacuum chamber for several weeks. The trapped air bubbles can therefore be extracted from the pores of the rock sample and the space will be replaced by de-aired water.

The experimental setup for hydraulic pulse tests is schematically shown in Figure 4.4. The saturated Cobourg Limestone sample is submerged in water reservoir without any compressive or confining stresses. The water temperature is measured using an Omega thermocouple (Type K Hermetically Sealed Tip Insulated Design with 24 AWG Stranded). De-aired water is pumped into the interior cavity for building up the hydraulic pulses. Rigid metal pipes have been utilized for connecting the Quizix Precision Pump (Model QX-6000 providing flow rate of 0.001–50 ml/min) with the pressurization system. The pulse decay within cavity is monitored with a Honeywell pressure transducer (Model TJE with 300 psi range and 0.1% accuracy) and readings are taken through the DasyLab data acquisition system.

4.1.2 Test procedures

The experimental procedures for performing hydraulic pulse tests on cuboidal samples of Cobourg Limestone can be summarized as follows:

(a) The rock sample was saturated under vacuum condition for 7 days. The saturated cuboidal sample was then submerged in water in the testing chamber to allow for 24-hour dissipation of residual negative pressure.

(b) In order to eliminate any trapped air bubbles from the central cavity and fittings, vacuum suction was applied to the de-airing pipe before conducting transient pulse tests on Cobourg Limestone sample. The cavity pressure was maintained at -86 kPa by a Venturi pump. During the vacuum suction process, the water inlet valve should be closed while the de-airing valve that is connected to the Venturi pump should stay open. The vacuum suction was turned off after a 24-hour de-airing period and a further 24-hour should be allowed for complete dissipation of the residual negative pressure within the rock matrix.

(c) The hydraulic pulse was established by pumping de-aired water into the fluid-filled cavity at a constant flow rate of 0.2 ml/min ~ 2 ml/min. Upon attainment of the prescribed internal pressure, the water inlet valve was closed and the pump was stopped immediately. The cavity pressure decay was monitored with a pressure transducer and readings were taken every 1 s.

(d) The data acquisition was terminated after 2 hours and the de-airing valve was opened to allow for 6-hour dissipation of any excess pore pressures that remained in the sample.

(e) The procedure was repeated for different hydraulic pulses to obtain repeatable results.

4.2 Theoretical and Computational Modelling

The interpretation of hydraulic pulse test relies on the computational simulation of the fluid pressure decay process within pressurized cavity. The coupled hydro-mechanical modelling of

hydraulic pulse diffusion through saturated rock matrix should take into consideration the deformable porous skeleton and compressible permeating fluid.

4.2.1 Governing equations

According to Darcy's Law, the fluid velocity within a hydraulically isotropic rock can be expressed in the form

$$\mathbf{v} = -\frac{K}{\mu}\nabla p(\mathbf{x},t) \tag{4.1}$$

where $p(\mathbf{x},t)$ represents the pore water pressure distribution, μ is the dynamic viscosity of water, and K denotes the intrinsic permeability of the rock.

The mass conservation law for a deformable porous medium saturated with a compressible fluid states that

$$S\frac{\partial p(\mathbf{x},t)}{\partial t} + \nabla\cdot(\mathbf{v}) = 0 \tag{4.2}$$

where S ($=nC_w+C_{eff}$) gives the specific storage of the porous medium, n is the rock porosity, C_w represents the compressibility of the pore water, and C_{eff} denotes the effective compressibility of the porous skeleton.

Therefore, the governing equation for the position- and time-dependent fluid pressure within the cuboidal water-saturated rock matrix is given by

$$\left(\frac{K}{\mu(nC_w + C_{eff})}\right)\nabla^2 p(\mathbf{x},t) = \frac{\partial p(\mathbf{x},t)}{\partial t} \tag{4.3}$$

The kinematic constraint for the pressurized fluid within the cavity requires that the rate at

which water moves from the pressurized cavity into the porous medium, as expressed by Darcy's Law applied to the fluid-rock interface, must be identical to the volume expansion rate of the cavity fluid resulting from hydraulic pulse decay, written as

$$\iint_{S_D} \frac{K}{\mu} \nabla p dS = V C_w \left(\frac{\partial p}{\partial t} \right) \Bigg|_{\text{cavity}} \tag{4.4}$$

where S_D represents the contact area of fluid-rock interface and V is the volume of pressurized fluid within the cylindrical cavity and connected fittings.

The initial conditions for the pressurized cavity and rock matrix are specified as

$$p(\mathbf{x},0) = \begin{cases} p_0, & \text{cavity} \\ 0, & \text{matrix} \end{cases} \tag{4.5}$$

which indicate that the cavity fluid is subjected to an hydraulic pulse p_0, and the rock matrix contains no residual hydraulic gradients before testing.

For the boundary condition at epoxy sealing interface, the zero water flow through the rock surface (null Neumann boundary condition) is specified as

$$\frac{\partial p}{\partial z} = 0 \tag{4.6}$$

For the other surfaces exposed to water reservoir, null Dirichlet boundary conditions have been specified as

$$p(\mathbf{x},t) = 0 \tag{4.7}$$

4.2.2 Entrapped air bubbles

The presence of entrapped air within the cavity can alter the compressibility of the pressurized

fluid (Schuurman, 1966; Fredlund, 1976; Nguyen and Selvadurai, 1995; Scherer, 2008), which may significantly influence the cavity pressure decay pattern under various levels of hydraulic pressure pulses (Selvadurai and Najari, 2015). As fluid pressure builds up in the cavity, the entrapped air bubbles are simultaneously compressed. Because of the much higher compressibility for air, the effective compression of the air-water mixture can be appreciably increased and thus the pressurization process is slowed down. On the other hand, as the hydraulic pulse decays in the cavity, entrapped air bubbles can expand in volume and therefore the pressure dissipation is significantly delayed. Consequently, the theoretical interpretation of transient pulse tests may lead to an inaccurate estimation of the rock permeability.

A procedure for considering air content in the pressurized cavity has been developed by Selvadurai and Najari (2015), who have conducted computational modelling of transient pulse test at different air fractions and variable initial pulse pressures. In order to account for the effects of entrapped air on hydraulic pulse tests, assumption is made that the air inclusions in the pressurized fluids are in the form of distributed bubbles and air solubility in water is not considered. For a certain volume of air-water mixture (V_t) consisting of pure water (V_w) and entrapped air bubbles (V_a), the air fraction is defined as

$$\phi = \frac{V_a}{V_a + V_w} \tag{4.8}$$

The isothermal compressibilities of pure water and air are defined as

$$C_a = -\frac{1}{V_a}\frac{dV_a}{dp} \quad \text{and} \quad C_w = -\frac{1}{V_w}\frac{dV_w}{dp} \tag{4.9}$$

By neglecting the influences of water surface tension and vapor pressure within air bubbles,

the pressures for both air and water are assumed to be identical. The equivalent compressibility of air-bearing fluids can be expressed as

$$C_{eq} = -\frac{1}{V_t}\frac{dV_t}{dp} = -\frac{1}{V_a + V_w}\frac{d}{dp}(V_a + V_w) \tag{4.10}$$

with

$$-\frac{1}{V_a + V_w}\frac{dV_a}{dp} = -\frac{V_a}{V_a + V_w}\frac{1}{V_a}\frac{dV_a}{dp} = \phi C_a \tag{4.11a}$$

$$-\frac{1}{V_a + V_w}\frac{dV_w}{dp} = -\frac{V_w}{V_a + V_w}\frac{1}{V_w}\frac{dV_w}{dp} = (1-\phi)C_w \tag{4.11b}$$

Therefore, the compressibility of air-water mixture can be estimated as

$$C_{eq} = \phi C_a + (1-\phi)C_w \tag{4.12}$$

Based on Boyle's Law that describes the volume-pressure relationship for ideal gases under isothermal conditions, the compressibility of air can be derived as

$$PV_a = \text{const} \Rightarrow PdV_a + V_a dP = 0 \Rightarrow C_a = -\frac{1}{V_a}\frac{dV_a}{dp} = \frac{1}{P} \tag{4.13}$$

where $P = p + P_0$ denotes the absolute air pressure, P_0 = 101 kPa represents the atmosphere pressure, and thus $dP=d(p+P_0)=dp$. Assuming that the total volume of the pressurized cavity remains approximately constant during hydraulic pulse tests, the air fraction change under different pressures can be derived as

$$\left.\begin{aligned} P_0 V_a^0 &= PV_a \\ \phi_0 &= \frac{V_a^0}{V_w + V_a} \end{aligned}\right\} \Rightarrow \phi = \frac{V_a}{V_w + V_a} = \frac{\frac{P_0}{P}V_a^0}{V_w + V_a} = \frac{P_0}{P}\phi_0 \tag{4.14}$$

where V_a^0 is the initial volume of entrapped air within cavity at atmosphere pressure, and ϕ_0 gives the initial air fraction.

Thus, the equivalent compressibility of the air-water mixture can be expressed as

$$C_{eq} = \frac{P_0}{P^2}\phi_0 + (1 - \frac{P_0}{P}\phi_0)C_w \tag{4.15}$$

The influence of trapped air bubbles on the compressibility of a pressurized air-water mixture is shown in Figure 4.5. The compressibility of pure water is specified as $C_w = 4.54\times10^{-10}$ Pa^{-1} under standard temperature and pressure (White, 1986). It is clearly observed that air inclusions can significantly change the fluid compressibility, e.g. 1% air fraction may increase fluid compressibility by two orders of magnitude at zero hydraulic pressure. As the fluid pressure increases, the compressibility of the air-water mixture decreases and tends to approach pure water compressibility.

4.2.3 Numerical simulation

In order to quantitatively account for the influences of trapped air bubbles and pressure-dependent fluid compressibility on the results of hydraulic pulse tests, we have used the Finite Element procedures available in COMSOL™ to conduct computational modelling of the pressure decay in the pressurized cavity. The pore pressure dissipation driven by the initial pressure difference between the pressurized cavity and saturated rock matrix can be easily modeled using the transient-diffusion equations (described by Equations 4.1–4.3) with a specific storage defined by

$$S = \begin{cases} nC_w + C_{eff} & \text{saturated rock matrix} \\ C_{eq} & \text{pressurized cavity} \end{cases} \tag{4.16}$$

Here, the fluid-filled cavity will be modeled as a porous material with permeability

substantially higher than the tested rock ($K_w = 1\times10^{-12}$ m^2) and porosity equal to 1 (Selvadurai and Jenner, 2013). The accessible pore space in the rock matrix is considered to be fully saturated after the vacuum saturation process and no air is present within the pore water. The boundary of the fluid-rock interface is assumed to be fixed and therefore there is no expansion of the pressurized fluid domain. Assuming that the pressurized fluid is simulated as an equivalent cylindrical column and the cross-section area is same with the contact area of the fluid-rock interface, the height for cavity water can therefore be calculated (Table 2.1).

As an illustrative example, the 3-D finite element model for sample S6-6 is shown in Figure 4.6. Due to symmetry, only one quarter of the cuboidal rock sample is considered in the numerical analysis. The mesh contains 549566 tetrahedral elements with 752154 degrees of freedom. The proposed modelling scheme requires extremely fine meshing in the pressurized cavity region in order to accurately simulate the hydraulic pulse decay process. We choose typical material properties for Cobourg Limestone as $C_{eff} = 7.211\times10^{-11}$ Pa^{-1}, $n = 0.01$, $K = 1\times10^{-20}$ m^2, and water viscosity $\mu = 1\times10^{-3}$ Pa·s at standard condition.

The modelling results for cavity pressure decay (p_0 = 500 kPa) under different initial air fractions (ϕ_0 = 0%, 0.1%, 1%) are shown in Figure 4.7a. The theoretical curve for pressure decay in the central pressurized cavity is very fast because of the small compressibility of pure water. However, due to the existence of air within water and the relatively higher compressibility of air-water mixture, the cavity pressure dissipation can be significantly delayed even with a rather small air fraction.

On the other hand, the amount of trapped air bubbles within the pressurized fluids can also

influence the establishment of hydraulic pulse. Since the cavity pressure buildup is supposed to be rapid and the rock permeability is relatively low, the instantaneous penetration of pressurized fluid into rock matrix during establishing hydraulic pulse can be neglected. Therefore, the governing ordinary differential equation for cavity pressure buildup can be written as

$$\frac{dp}{dt} = \frac{q}{C_{eq}V} \tag{4.17}$$

where q is the volumetric flow rate into the pressurized cavity, V denotes the cavity volume, and C_{eq} represents the equivalent compressibility of the air-water mixture defined by Equation 4.15.

The numerical outputs for cavity pressure buildup with a constant flow rate of 1 ml/min are shown in Figure 4.7b. The theoretical pressure buildup in the central cavity is rapid as a result of the low compressibility of pure water. The existence of air within water increases the compressibility of the air-water mixture, and correspondingly the cavity pressure buildup can be significantly delayed and become highly nonlinear.

4.3 Transient Test Results

The room temperature within the time of pulse decay was 24 ± 0.5 °C. In order to check the effectiveness of epoxy sealing, several sealing experiments were conducted on a water-filled stainless steel tube. The entire pressurization system was immersed under water for the purpose of eliminating any possible influences of ambient temperature changes. The pressure pulses

applied within the sealed steel tube were kept in the range of 400 to 500 kPa. The drop in the tube pressure is relatively small (less than 1%) over a time duration of 15000 s, as illustrated in Figure 4.8. This confirms that the Marine epoxy is a successful sealing technique for performing a hydraulic pulse test.

Transient tests were performed on Cobourg Limestone samples after vacuum de-airing. The typical results for sample S6-16 is shown here for the purpose of demonstrating permeability interpretation procedures. De-aired water, at a constant flow rate of 1 ml/min, was pumped into the fluid-filled cavity. The cavity pressure was allowed to increase to around 600 kPa level (543 kPa and 604 kPa). The time needed to attain the pressure pulse was recorded to be approximately 11 s for these transient tests. The experimental results for pressure decay within the pressurized cavity are compared with computational results in Figure 4.9. The computational estimates of cavity pressure decay are obtained for several choices of K ranging from 10^{-22} m^2 to 10^{-19} m^2 without considering the influence of trapped air. This graphical representation allows the target permeability range to be narrowed down. The exact value of the permeability can be conveniently determined by closely matching the numerical calculations with experimental pressure decay curves. The permeability of Cobourg Limestone is estimated to be around 4.0×10^{-22} m^2.

The pressure-dependent compressibility of air-water mixture within the cavity contribute to the nonlinear pressure buildup and delayed pulse decay responses. The amount of trapped air within pressurized fluids can be estimated from the recorded cavity pressure build-up curves, as shown in Figure 4.10a. The same trapped air fraction of $\phi_0 = 0.5\,\%$ is obtained for the two

different flow rates (1 ml/min and 2 ml/min). Accounting for the influence of the air fraction on hydraulic pulse decay, the rock permeability is estimated to be 3.0×10^{-21} m^2 for cavity pressure of 600 kPa (Figure 4.10b). The trapped air fraction results in an order of magnitude difference in the estimation of the permeability.

For sample S6-6, the cavity pressure was allowed to increase to around 550 kPa level (549 kPa and 553 kPa) by pumping de-aired water into the fluid-filled cavity at a constant flow rate of 0.2 ml/min. The time needed to attain the pressure pulses was recorded to be around 6 s. The experimental cavity pressure decay curves are compared with numerical predictions in Figure 4.11. The permeability of Cobourg Limestone is estimated to be around 2.6×10^{-21} m^2 without considering the effects of trapped air fraction. Based on the cavity pressure build-up curves, the air bubble fraction is estimated to be $\phi_0 = 0.03\,\%$ after vacuum de-airing of the fluid-filled cavity (Figure 4.12a). This air fraction is then used to simulate the hydraulic pulse decay process and the rock permeability is estimated to be 4.0×10^{-21} m^2 for cavity pressure of 550 kPa (Figure 4.12b). A perfect match between the experimental results and numerical outputs has been observed for the transient tests. Since the air fraction is rather small, the permeability estimations are quite close to each other with or without a correction for the influence of the air fraction on the compressibility of the pressurized fluid.

4.4 Steady-state Tests

In order to verify the accuracy of the results obtained from transient tests, pressure controlled steady-state tests were also conducted on the same cuboidal samples of Cobourg Limestone.

The permeability can be estimated from the measured hydraulic responses of the equilibrium steady-state flow (cavity pressure and flow rate), the geometry of the cuboidal samples, and the associated boundary conditions for the experimental configuration.

4.4.1 Analytical and numerical modelling

For steady-state permeability test, the pore pressure distribution within the saturated rock matrix can be mathematically described by Laplace's equation

$$\nabla^2 p(\mathbf{x}) = 0 \tag{4.18}$$

Considering the experimental arrangement, the boundary conditions are shown in Figure 4.13. According to Selvadurai and Najari (2016), the permeability test in a partially cored cavity can be ideally considered as a combination of radial flow permeability test (Selvadurai and Selvadurai, 2007) and patch permeability test (Selvadurai and Selvadurai, 2010).

The analytical solution for axisymmetric radial flow within hollow cylinder can be adopted for estimating the radial flow within hollow cube, written as

$$Q = \frac{2\pi HK}{\mu \ln(b/a)} p_{\text{cavity}} \tag{4.19}$$

where p_{cavity} represents the interior cavity pressure and the equivalent outer diameter ($2b$) is written as

$$2b = \frac{4c}{\pi} \tag{4.20}$$

which is corresponding to the same flow surface analogy between hollow cylinder and hollow cube.

The half-space solution for the patch permeability test is written as

$$Q = \frac{4aK}{\mu} p_{\text{cavity}} \tag{4.21}$$

Therefore, the analytical solution for steady-state fluid flow through the pressurized cavity in this experiment can be approximately obtained as

$$Q = \left[\frac{2\pi H}{r \ln(b/a)} + 4 \right] \frac{rK}{\mu} p_{\text{cavity}} \tag{4.22}$$

Here, $F = \frac{2\pi H}{r \ln(b/a)} + 4$ is defined as the shape factor. For the proposed experimental configuration and the geometric dimensions, the analytical shape factor is calculated as F = 27.66 for S6-16 and F = 25.72 for S6-6.

In order to verify the analytical estimation, the finite element procedures available in COMSOL^{TM} are used to perform computational modelling of the steady-state fluid flow through the partially cored cuboidal sample. The modelling approach for transient pulse test as described in Section 4.2.3 is adopted here. Steady-state flow is induced by specifying constant inward fluid velocity $v_0 = q/(\pi a^2)$ at the upper surface of the pressurized cavity column. The Darcy flow parameters are chosen as q = 0.0001 ml/min, $K = 1\times10^{-20}$ m^2, and water viscosity $\mu = 1\times10^{-3}$ Pa·s at standard condition. The 3-D finite element model with pressure distribution is shown in Figure 4.14. Based on the numerical output, the shape factor can be obtained as F = 31.47 for S6-16 and F = 29.32 for S6-6. The differences between analytical and numerical shape factors are within 10 %. In the following interpretation of steady-state test results, the numerical shape factor is used for permeability estimation.

4.4.2 Test results

The same experimental setup for transient pulse test was used to conduct steady-state test, except that the Quizix Precision Pump was switched to "Paired constant pressure delivery" mode for maintaining constant cavity pressure. The volume of delivered water was monitored by recording the piston movement of Quizix pump and readings were taken every minute through the PumpWorks^{TM} Data Log. The proposed steady-state tests were repeated at different inlet pressures (350 kPa, 500 kPa and 650 kPa) and each test lasted about 3–5 days.

Typical results for the evolution of pump flow rate under constant cavity pressure are shown in Figure 4.15. At equilibrium state, the pumping flow rate is recorded to be around 0.00008 ml/min at cavity pressure of 650 kPa for S6-16 and 0.000049 ml/min at cavity pressure of 500 kPa for S6-6. Therefore, the permeability can be calculated to be 5.8×10^{-21} m^2 for S6-16 and 4.8×10^{-21} m^2 for S6-6, respectively. These permeability measurements agree very well with the transient test results after air bubble correction.

4.5 Permeability under Compressive Stress

The experimental configuration for steady-state permeability tests on cuboidal samples of Cobourg Limestone under compressive stresses is schematically shown in Figure 4.16. A compressive load is applied by the Yellow Frame (capacity of 900 kN) and the stress is considered to be normal to the bedding plane. The proposed compression-permeability test is conducted on sample S6-11. The analytical shape factor is calculated as F = 27.07 and the

numerical shape factor is obtained as F = 30.78 (Figure 4.17). At each loading state, the permeability tests should be repeated for two different cavity pressures.

The selected pressure-controlled steady-state test results are shown in Figure 4.18. The compression-permeability relationship is summarized in Fig. 4.19. The rock permeability decreased from 3.9×10^{-20} m^2 at 0 MPa to 1.1×10^{-20} m^2 at 15 MPa during the compressive loading process. Further loading up to 20 MPa is observed to cause an increase in permeability due to compressive damage. During the unloading process, the rock permeability showed clear hysteresis behavior. Upon complete unloading, the intact permeability was measured to be 2.1×10^{-20} m^2.

It's relatively difficult to apply confining stress around a cuboidal rock sample. Pan *et al*. (2015) developed a 3-D printed membrane to hold the cubic shale sample and applied confining stress in a conventional triaxial cell. Anisotropic permeability was measured by re-orienting the sample in the triaxial cell. Nasseri *et al*. (2014) measured the 3-D transport properties of sandstone cubes in an advanced true-triaxial regime. The variation of permeability anisotropy was examined under different 3-D stress conditions. Li *et al*. (2016) studied the permeability evolution of shale cubes under anisotropic true-triaxial stress states. The greatest permeability reduction was observed when increasing compression normal to the bedding plane.

4.6 Discussion

Despite great efforts taken to reduce air within the pressurized fluid, trapped air within the

cavity cannot be completely eliminated. The proposed hydraulic pulse tests have been conducted at pressure levels between 500 and 600 kPa. At this pressure range, the trapped air can drastically increase the compressibility of the pressurized fluids. Without considering the pressure-dependent compressibility of air-water mixture, the rock permeability can be significantly underestimated. Therefore, it is necessary to follow the pressure buildup during establishing hydraulic pulses and estimate the residual air fraction within cavity. However, for the conventional transient tests proposed by Brace *et al.* (1968), the hydraulic pulses may reach as high as 40 MPa. Since the compressibility of the air-water mixture approaches pure water compressibility under high pressure (Figure 4.5), the influences of trapped air on the decay pattern of cavity pressure can be neglected. Sealing may become a more critical problem for the high pressure hydraulic pulse test.

Compared with transient pulse test, the interpretation of steady-state hydraulic test is much more straightforward. The estimation of permeability requires only knowledge of the geometry, the associated boundary conditions and the hydraulic response. Nonetheless, the presence of trapped air may also influence the establishment of steady flow through saturated rock. The computational modelling results for inlet pressure evolution under a constant flow rate of 0.00002 ml/min is shown in Figure 4.20 (S6-6). The time required to reach equilibrium state ($p_{\text{cavity}} \cong 259\,\text{kPa}$ for $K = 4.0\times10^{-21}\,\text{m}^2$ and $T = 24\,^{\circ}\text{C}$) is estimated to be 4 days, 13 days, and 25 days for different initial air fractions of ϕ_0 = 0.1 %, 0.5 %, 1 %, respectively. It can be clearly observed that the test duration is highly depended on the amount of trapped air within the pressurized cavity. For this reason, the pressure-controlled steady-state tests are preferable.

The influence of entrapped air on permeability measurement has received scant attention in literature. Keller and Kamp (1992) presents a method for considering storage due to entrapped air in slug test analysis. They have found out that the air present in the gravel pack and/or formation surrounding the piezometer intake increases the storage of piezometer and thus retards the recovery of water levels due to the high compressibility of air. The delayed hydraulic response may lead to underestimation of permeability. Scherer (2008) accounts for the pressure-dependent compressibility of air-water mixture and investigates the effects of air inclusions within pore liquid on steady-state permeability test. The analysis results show that the time required to reach steady flow can be significantly increased by the presence of entrapped air within pore liquid. The general implication of these studies is that the pressurization system should be de-aired and the rock samples are completely saturated before conducting the permeability tests.

Finally, the permeability of intact Cobourg Limestone samples is measured to be in the range of $[3, 39]\times10^{-21}$ m^2 in this study. Experiments have also been conducted by former group members to examine the intact permeabilities of argillaceous Cobourg Limestone. Axial flow hydraulic pulse tests are performed by Selvadurai *et al.* (2011), who have reported very low values for intact permeability of Cobourg Limestone as $[2, 75]\times10^{-23}$ m^2. Selvadurai and Jenner (2013) conduct radial flow permeability tests on hollow cylinders and estimate the in-plane permeability of intact Cobourg Limestone to be in the wide range of $[1, 1680]\times10^{-22}$ m^2. Selvadurai and Najari (2016) test cylindrical samples of Cobourg Limestone with partially cored cavity and measure the intact permeability as $[1, 40]\times10^{-20}$ m^2.

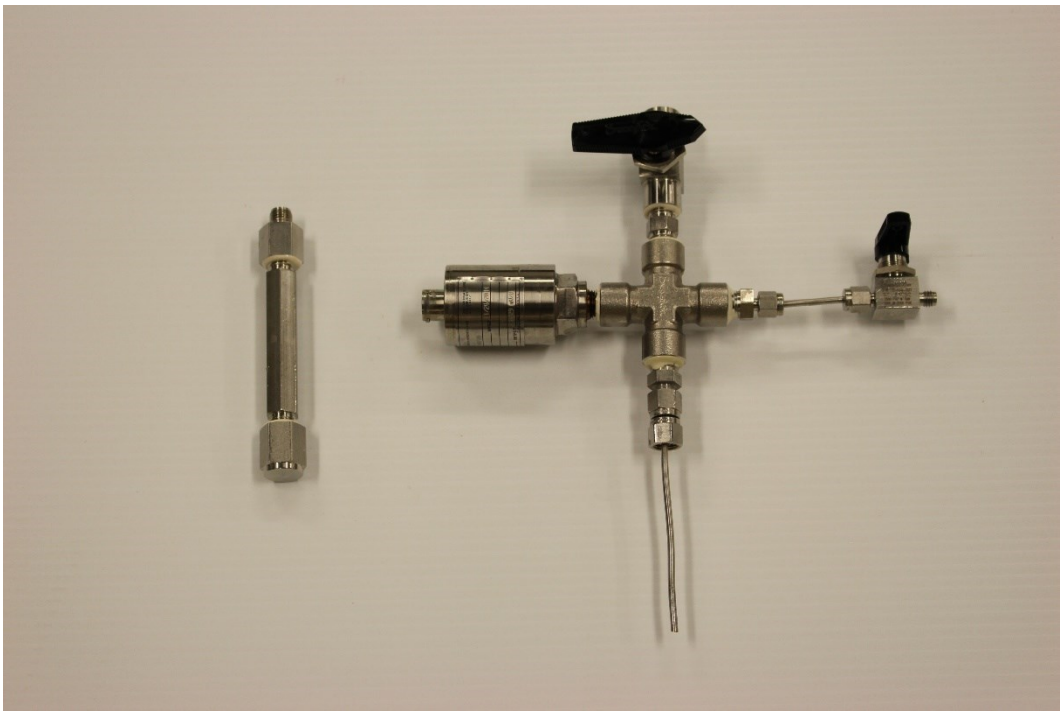

Figure 4.1 Pressurization system

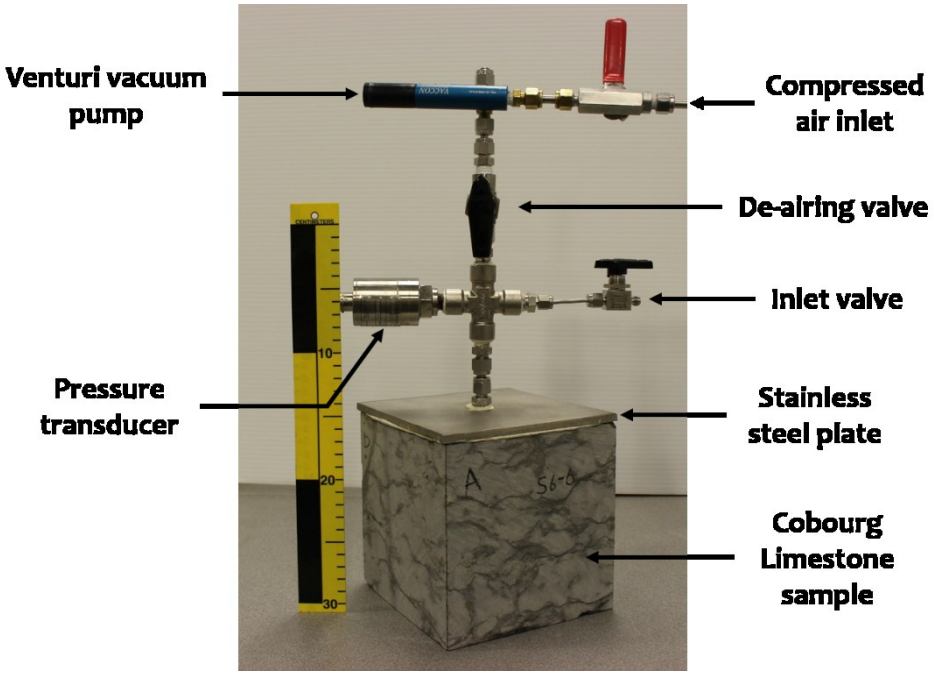

Figure 4.2 Sample assembly

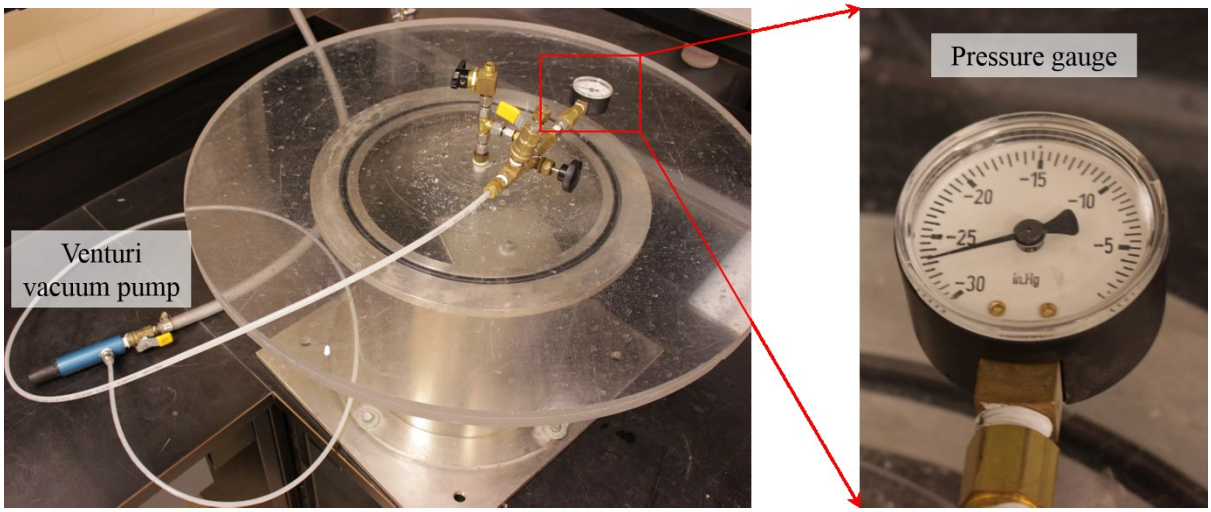

Figure 4.3 Vacuum chamber

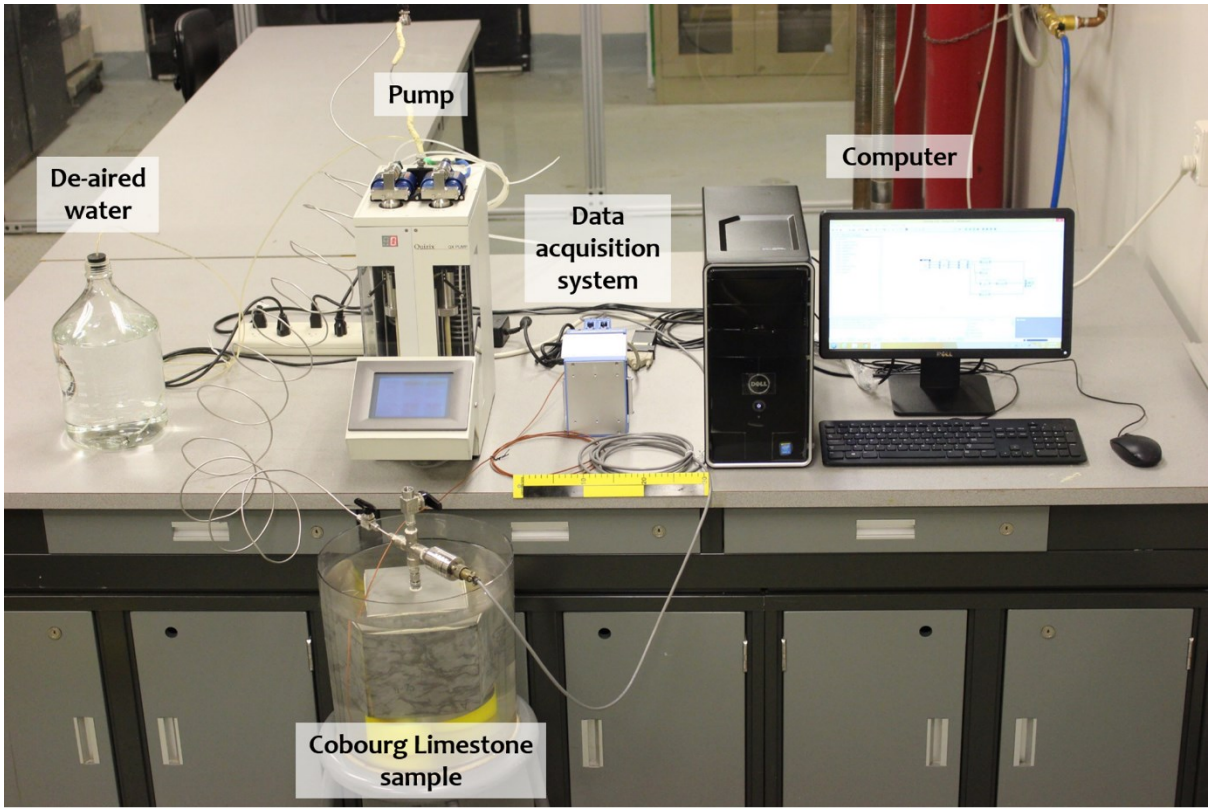

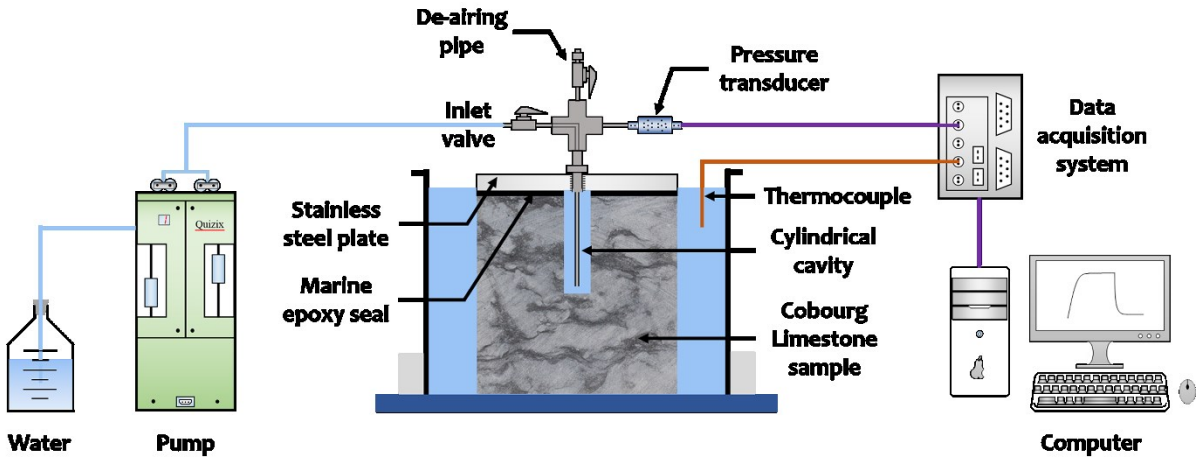

Figure 4.4 Experimental setup for hydraulic pulse test

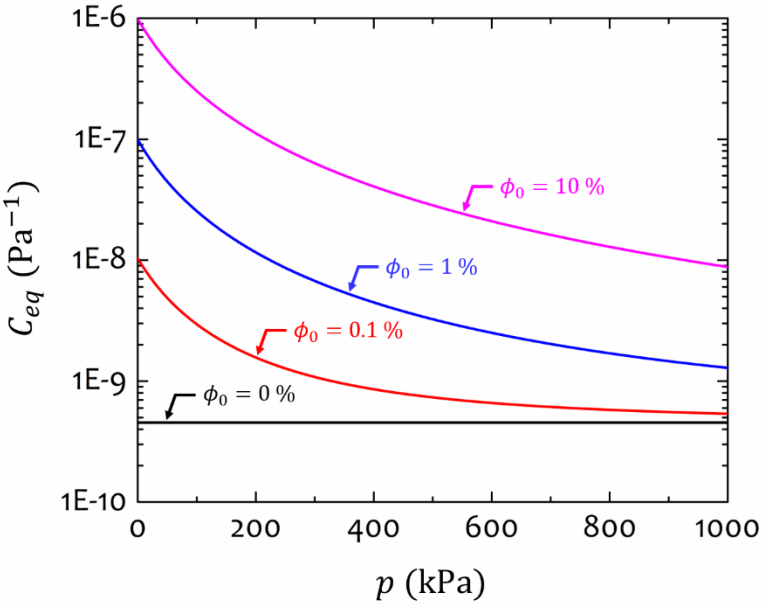

Figure 4.5 Compressibility of air-water mixture within pressurized cavity

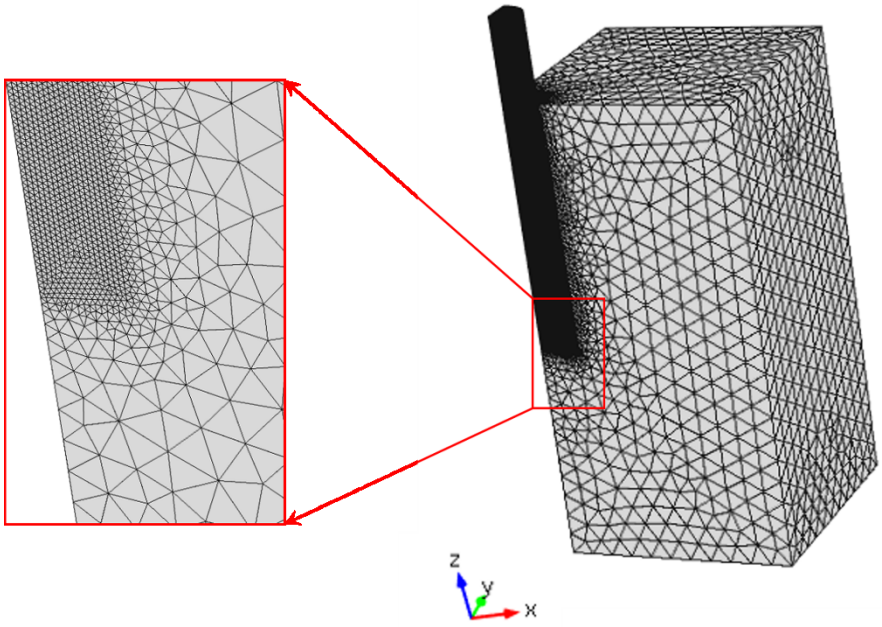

Figure 4.6 3-D finite element model for hydraulic pulse test

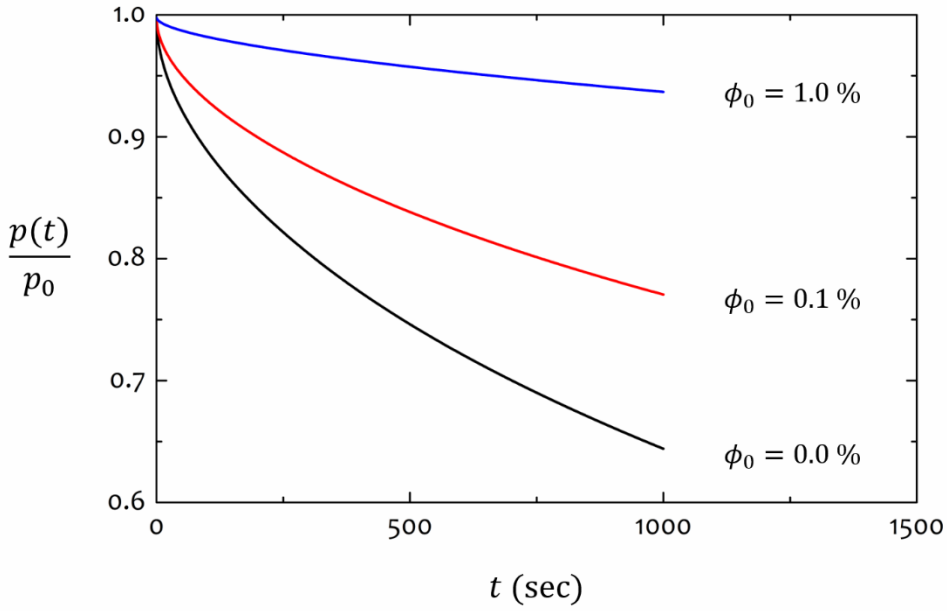

(a) Hydraulic pulse decay

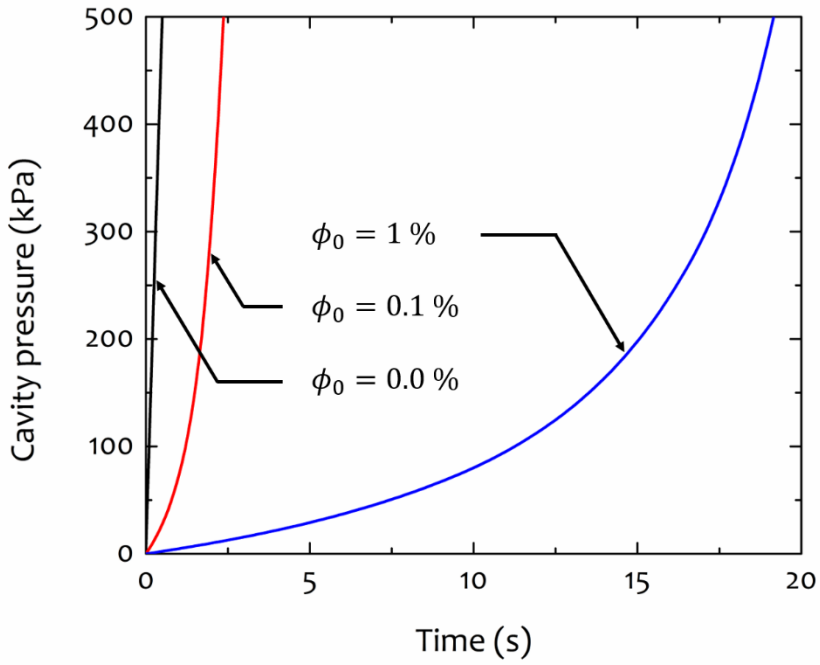

(b) Cavity pressure buildup

Figure 4.7 Influence of trapped air on transient pulse test

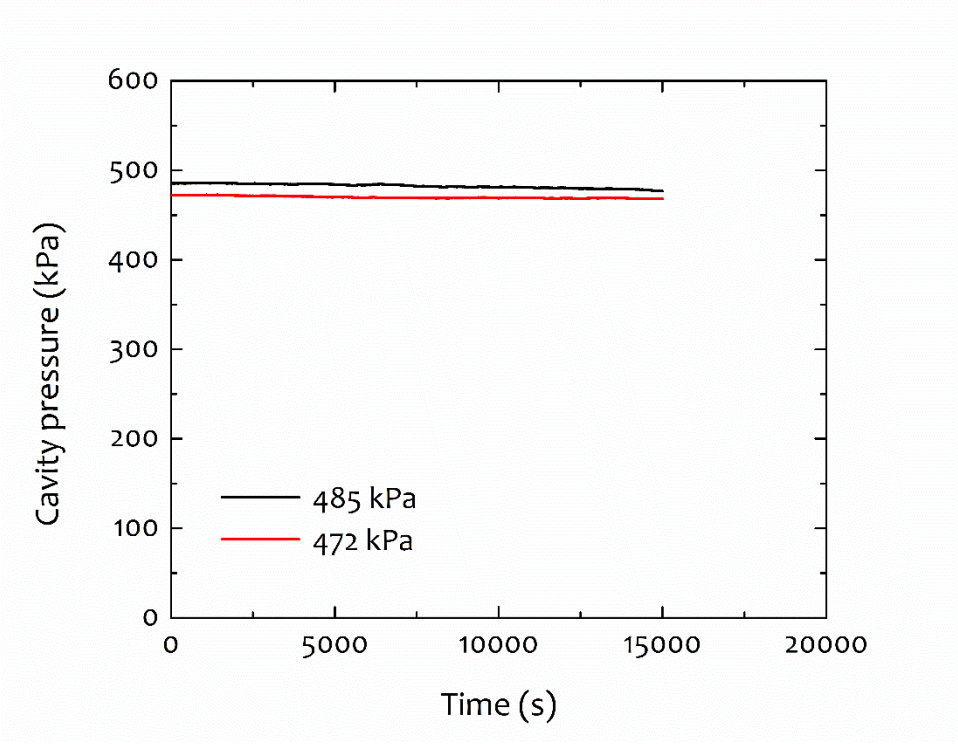

Figure 4.8 Sealing test results

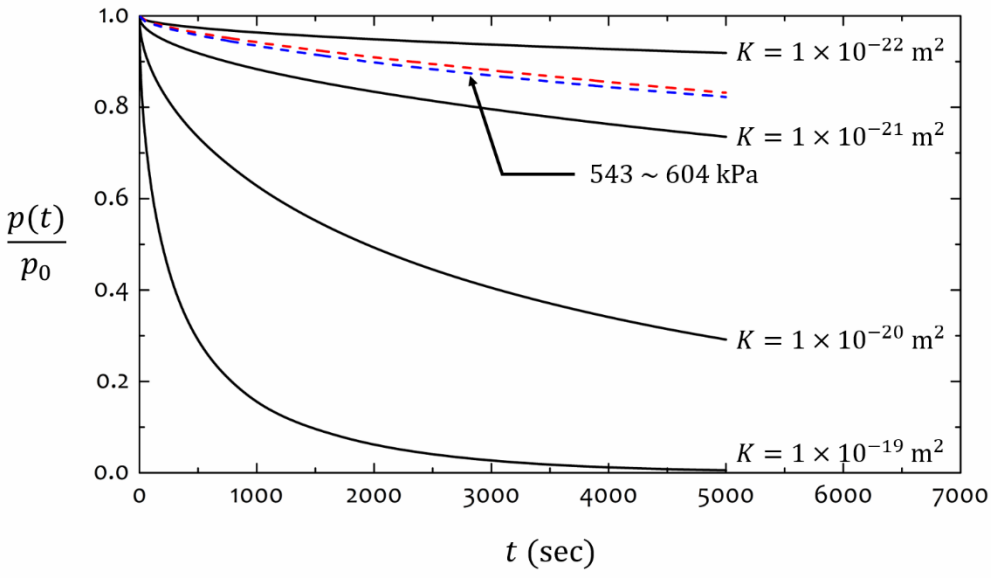

Figure 4.9 Transient test results for S6-16

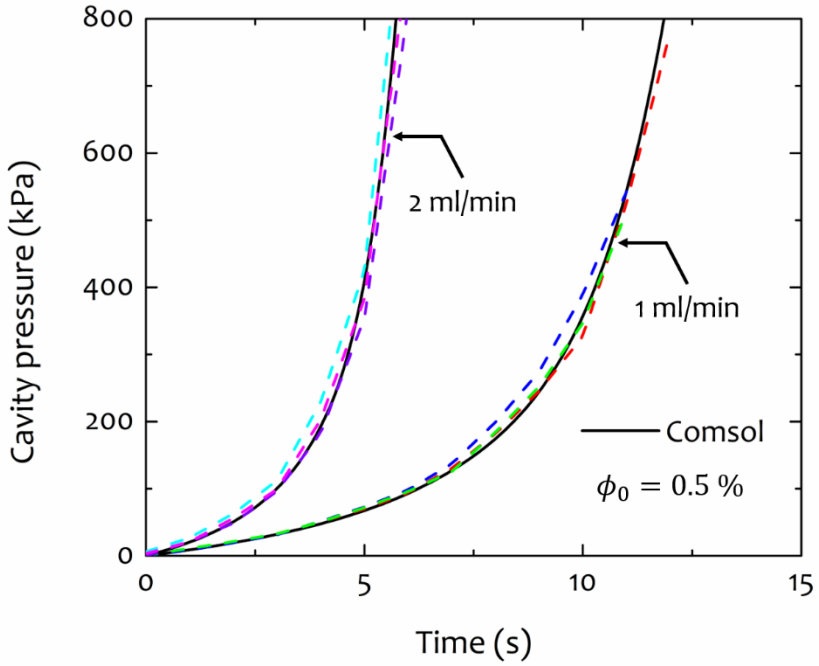

(a) Cavity pressure buildup

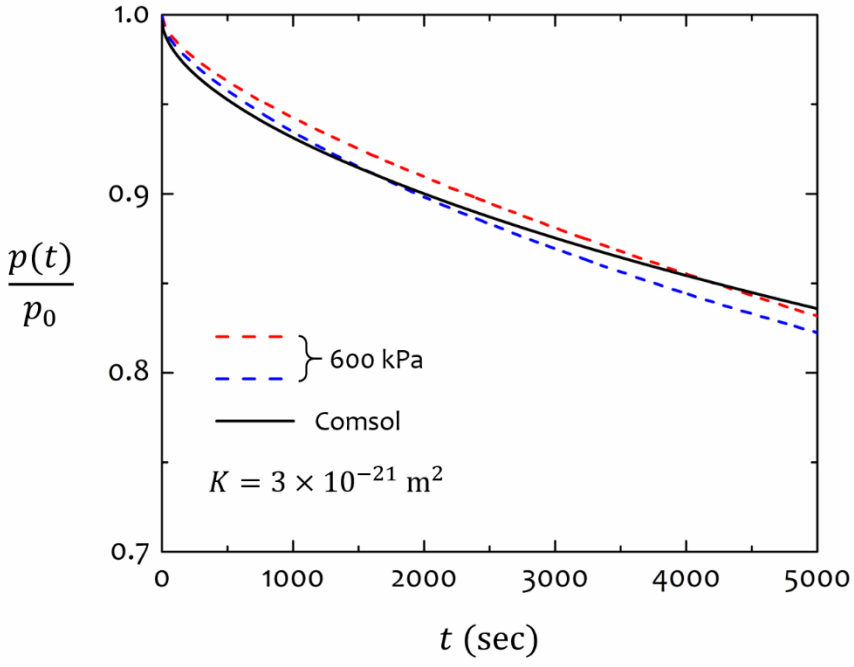

(b) Pulse decay matching

Figure 4.10 Numerical interpretation of transient test results for S6-16

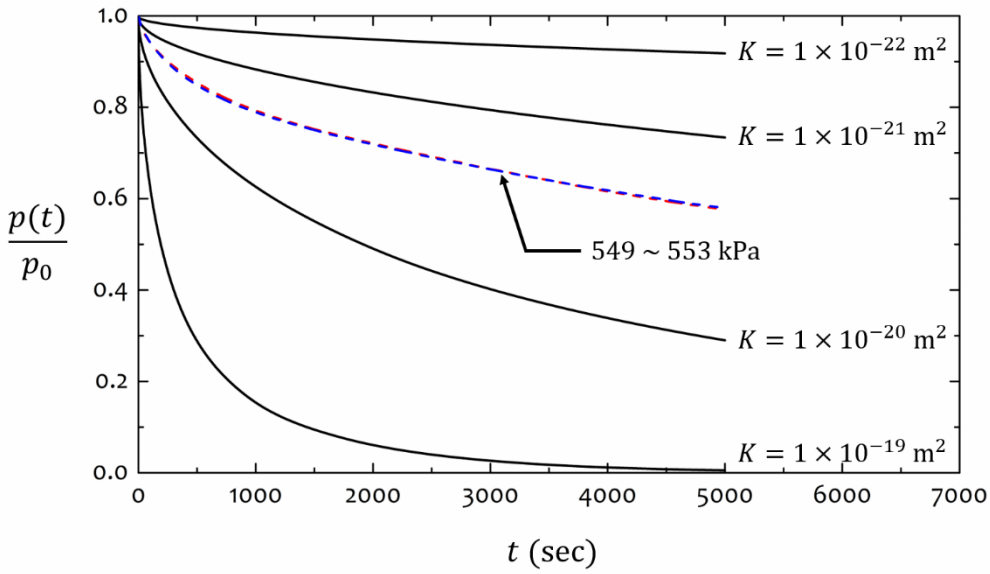

Figure 4.11 Transient test results for S6-6

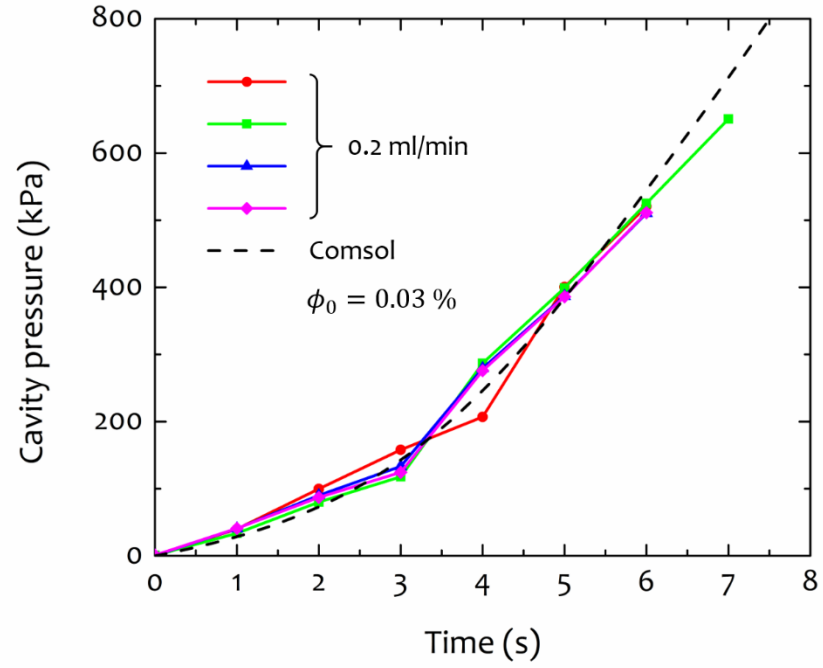

(a) Cavity pressure buildup

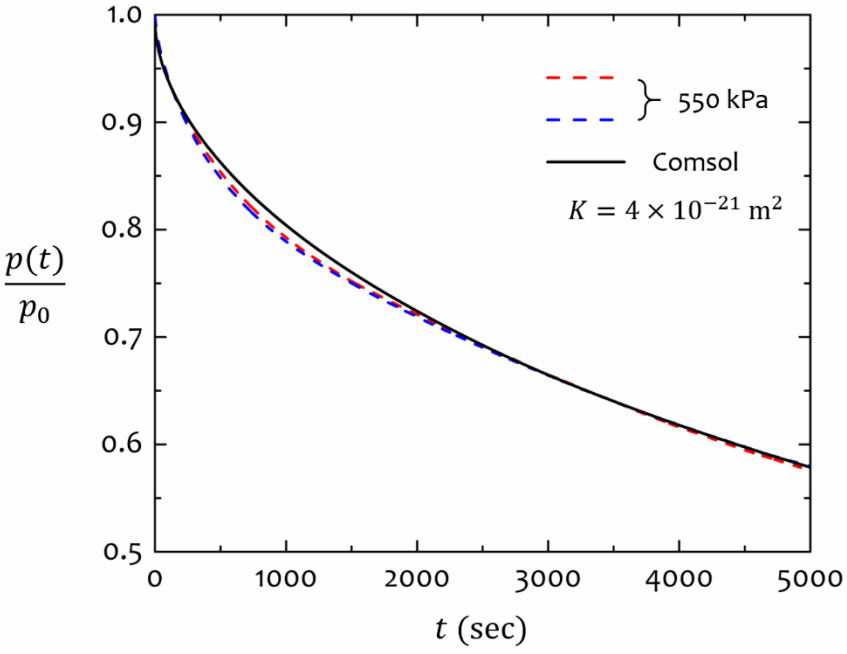

(b) Pulse decay matching

Figure 4.12 Numerical interpretation of transient test results for S6-6

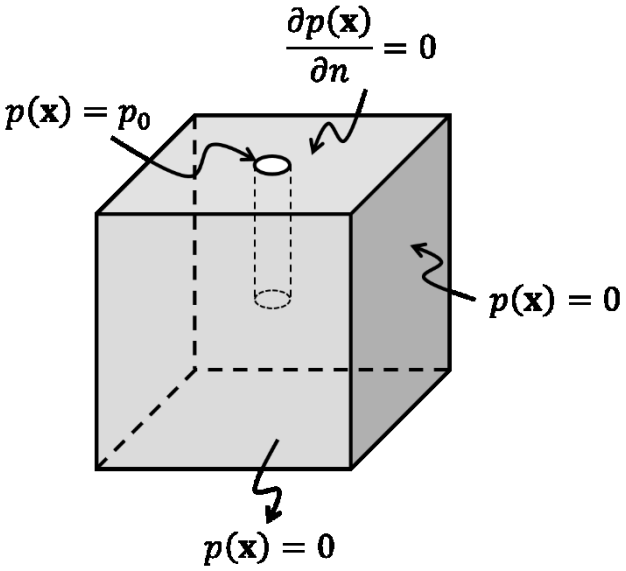

Figure 4.13 Boundary conditions for steady-state modelling

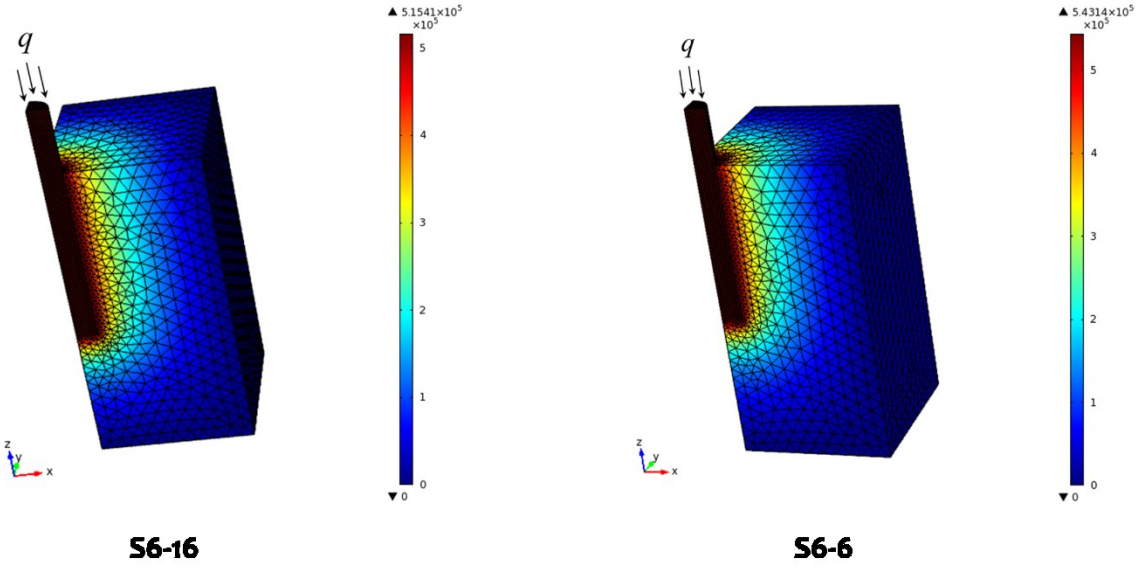

Figure 4.14 3-D finite element model for steady-state tests (Pressure: Pa)

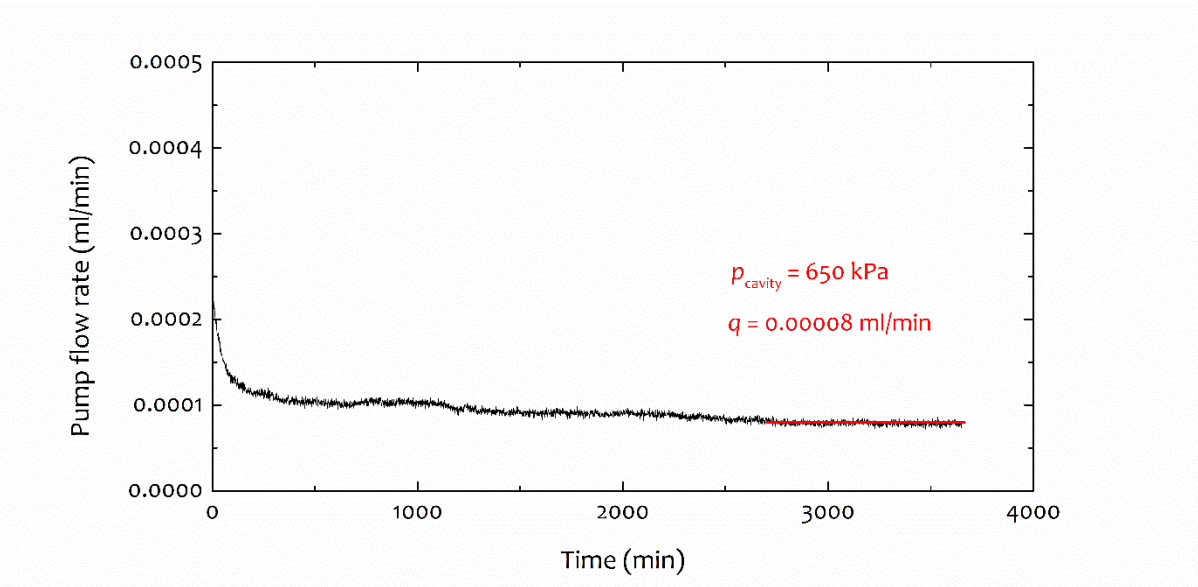

(a) For S6-16

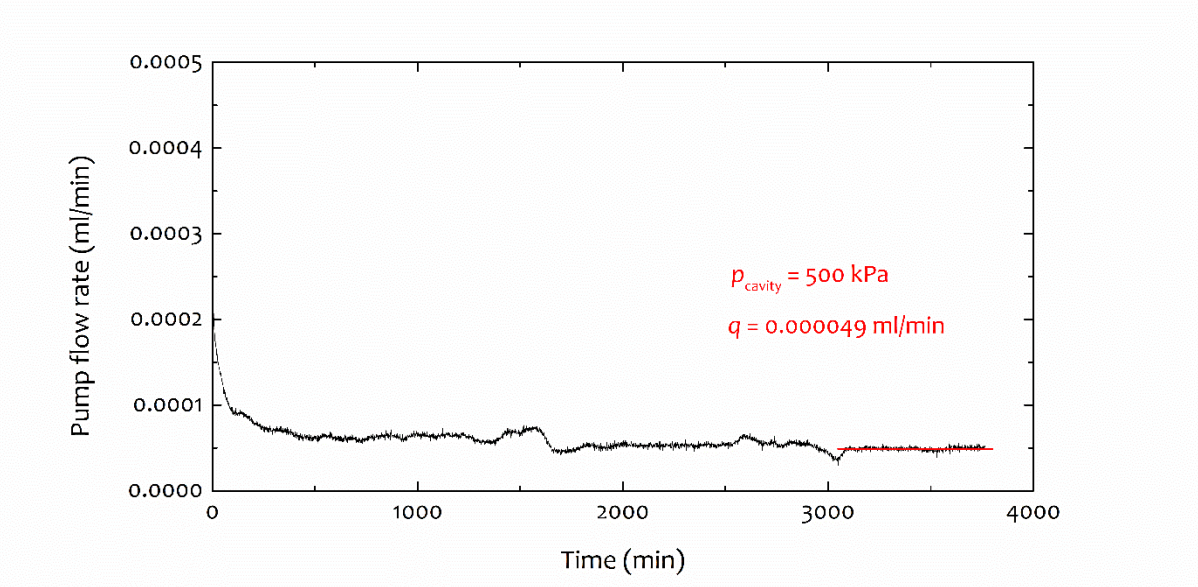

(b) For S6-6

Figure 4.15 Steady-state test results for intact Cobourg Limestone

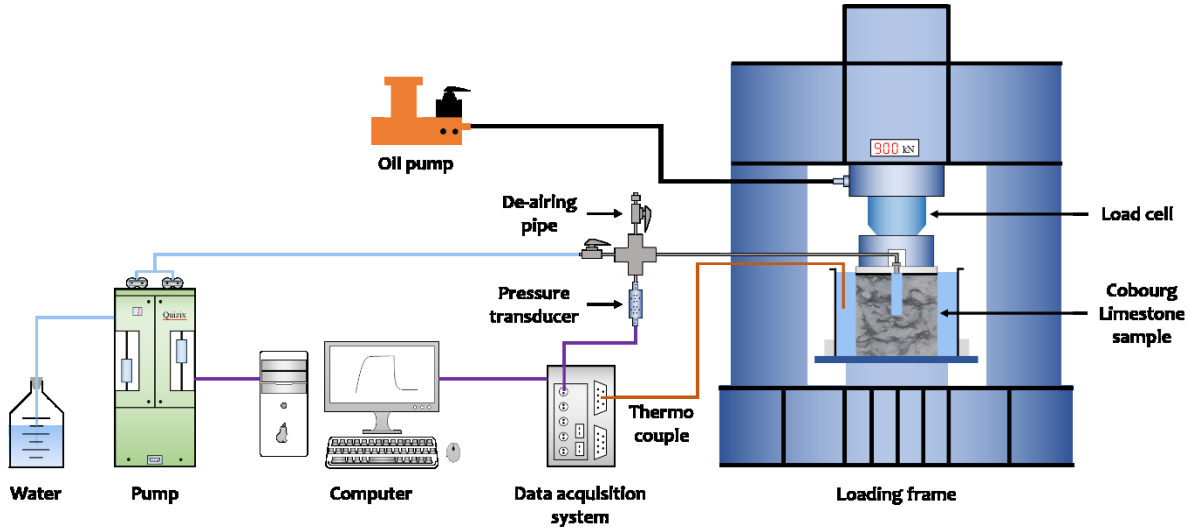

Figure 4.16 Experimental setup for steady-state test under compression

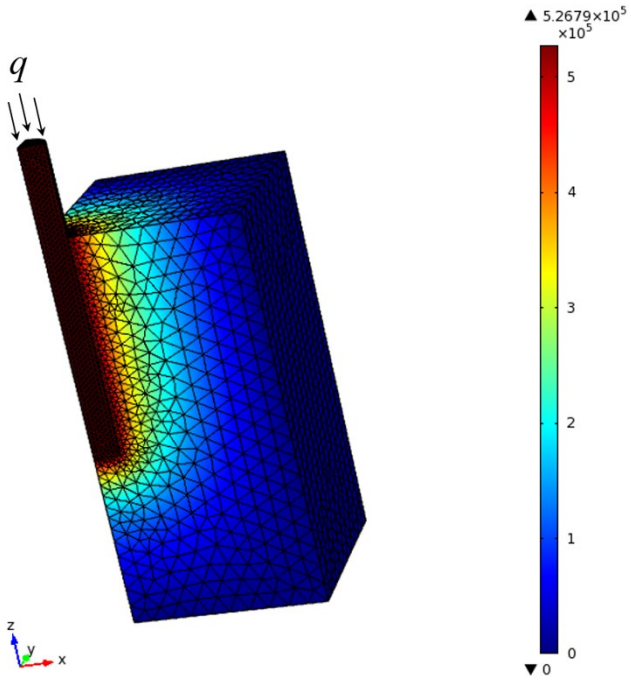

Figure 4.17 3-D finite element model for S6-11 (Pressure: Pa)

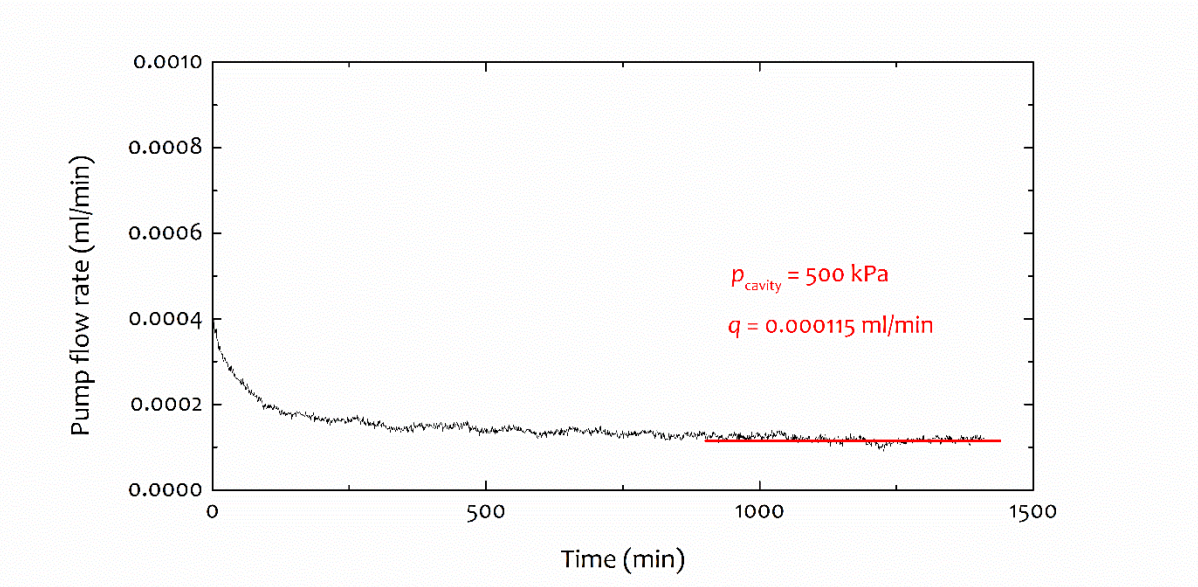

(a) 15 MPa loading

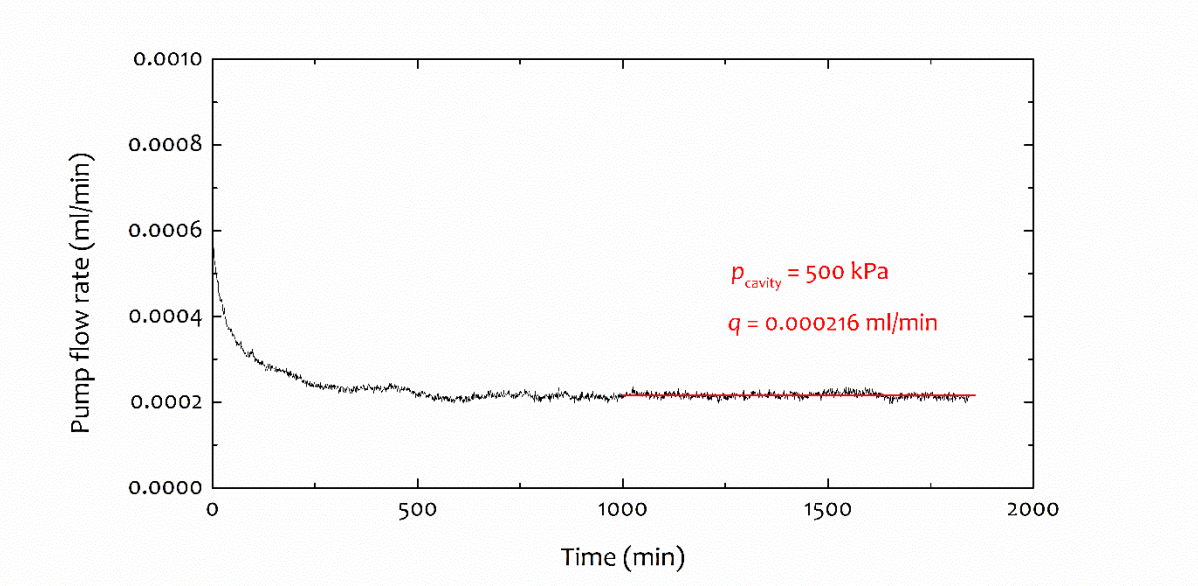

(b) 0 MPa unloading

Figure 4.18 Steady-state test results for S6-11 under compression

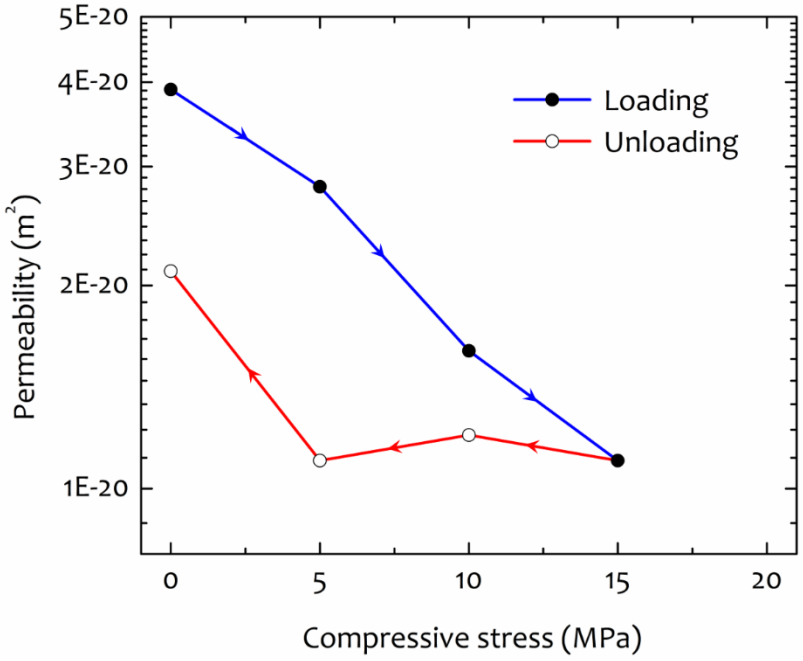

Figure 4.19 Permeability of intact cuboidal sample under compressive loading

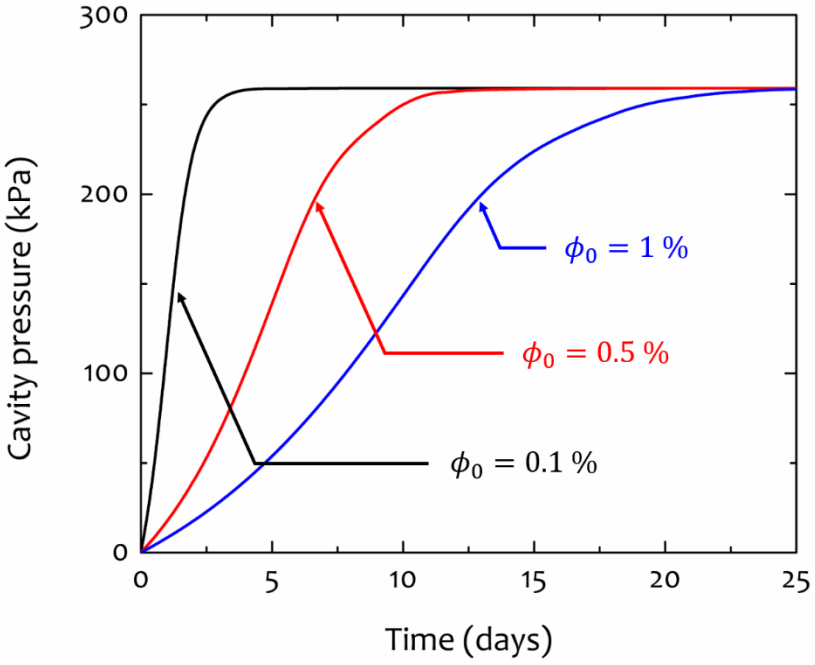

Figure 4.20 Influence of trapped air on steady-state permeability test

CHAPTER 5
FRACTURE PERMEABILITY

In fractured argillaceous geological formations, fluid flow occurs mainly in the fracture network. In the context of nuclear waste disposal, the ability of fractured rock to transport ground water as well as radionuclides is governed by the hydraulic conductivity of a single fracture under variable stress states. In order to measure the fluid flow properties of a single fracture, steady-state radial flow tests have been conducted on fractured cuboidal samples of Cobourg Limestone.

5.1 Sample Preparation – Installation of Fracture

In this study, artificial tensile fractures are created in cuboidal samples of the Cobourg Limestone containing a partially drilled cavity to conduct fracture permeability test. The three intact samples (S6-6, S6-11, and S6-16) used in the transient pulse tests are fractured. In order to introduce a flat fracture normal to the axis of the cavity, a splitting test is performed to crack the cube (Figure 5.1). The fracturing procedures can be described as follows:

(a) Circumferential lines, indicating the fracture plane perpendicular to the cavity axis, are marked around the mid-plane of the cuboidal surfaces.

(b) Four pairs of Demec points are glued to opposite side surfaces of the cuboidal sample, with each pair located at a distance of around 2 inch across the potential fracture plane. This allows for the precise re-assembly of the fractured rock sample as well as accurate measurement of initial fracture aperture.

(c) An elastic strip is tightened around the cuboidal sample. This method can prevent relative movements between separated parts of fractured rock, which could cause unwanted asperity shear and breaking particles.

(d) Two steel rods with 6-mm diameter and 200-mm length are placed along the mid-plane lines. Compressive load is applied by Compression Testing Machine (Test Mark CM-2500 with capacity of 250,000 lbs) to produce maximum tensile stress along mid-plane and to generate tensile fracture propagating through the rock sample.

(e) The initial fracture aperture is measured with Demec Gauge, which can measure the distance between two demec points with an accuracy of 0.00127 mm. The measurement difference before and after fracturing is recorded as the initial fracture aperture.

The initial aperture of the fracture, the peak compressive load and the calculated splitting tensile strength of Cobourg Limestone cubes are summarized in Table 5.1. The photographs of rough fracture surfaces and fracture orientation are shown in Figure 5.2 and Figure 5.3, respectively.

5.2 Steady-state Test Procedures

The experimental procedures for performing steady-state radial flow tests on fractured cuboidal samples of Cobourg Limestone are summarized as follows:

(a) The fractured cuboidal sample is separated and the fracture surfaces are washed with water in order to remove any debris. The cracked sample is reassembled by matching pairs of demec points. The rock sample is then placed into the testing chamber with the fracture submerged under water.

(b) The pump is connected to the pressurization system of the cuboidal rock sample. Before compressive load is applied, a nominal water flow is pumped into the cylindrical cavity in order to saturate the void space of the fracture.

(c) A compressive load is applied by the Loading Frame (Capacity of 900 kN) to produce a normal stress on the fracture plane.

(d) A constant water flow is applied to the cylindrical cavity and the cavity pressure is allowed to increase and reach a steady state. The evolutions of both cavity pressure and temperature are monitored throughout the test.

(e) The steady-state test is repeated for consecutive loading and unloading cycles in order to study the hysteresis behavior of fracture permeability.

The experimental setup for steady-state radial flow tests on fractured Cobourg Limestone cubes is schematically shown in Figure 5.4.

5.3 Analytical Modelling

The fracture permeability depends on the geometric parameters of the fracture, including aperture distribution, asperity contact area, and tortuosity. Fracture roughness can cause energy dissipation due to frictional slip during fluid flow across fracture surface. Fluid flow through fracture can be approximately described by the parallel plate model (Snow, 1965), as illustrated in Figure 5.5. Considering the very low permeability of intact Cobourg limestone (10^{-21} m^2), the fluid flow through the undamaged rock matrix is negligible compared to flow through the fracture. Therefore, the intact rock matrix is assumed to be impervious and the intrinsic permeability of the fracture (aperture λ) can be expressed as

$$K = \frac{1}{12}\lambda^2 \tag{5.1}$$

The cubic law for radial flow within the hollow cylindrical fracture (Witherspoon *et al*., 1979; Raven and Gale, 1985; Selvadurai, 2015) can be adopted to estimate the axisymmetric flow in this experiment, written as

$$Q = \frac{\pi(p_{in} - p_{out})\lambda^3}{6\mu \ln(b/a)} \tag{5.2}$$

where $b = \sqrt{c^2/\pi}$ is the equivalent outer radius corresponding to the same fracture flow area analogy between hollow cylinder and hollow cube, p_{in} and p_{out}(=0) represent the central cavity pressure and external surface pressure, respectively. The hydraulic fracture aperture can then be estimated as

$$\lambda = \left(\frac{6\mu Q \ln(b/a)}{\pi(p_{in} - p_{out})} \right)^{1/3} \tag{5.3}$$

and the fracture permeability expressed as

$$K = \left(\frac{\mu Q \ln(b/a)}{4\sqrt{3}\pi(p_{in} - p_{out})} \right)^{2/3} \tag{5.4}$$

In order for the cubic law to be applicable to the estimation of fracture permeability, it is essential that the entire fracture be fully saturated and the flow velocity be within the limits that ensure laminar flow. The Reynolds number, defined as the ratio of inertia force to viscous force during fluid flow, is often utilized to describe the transition from linear laminar flow to nonlinear turbulence flow. The critical Reynolds number that characterizes the onset of nonlinear flow resulting from fracture roughness and turbulence is reported to be between 10 to 100 in literature (Zimmerman and Yeo, 2000).

For radial flow in fracture, the Reynolds number is expressed as

$$\mathrm{Re} = \frac{\rho \mathrm{V} D}{\mu} \tag{5.5}$$

where ρ is the fluid density, μ denotes the dynamic viscosity of water, V gives the average fluid velocity, and $D = 2\lambda$ represents the characteristic dimension of fracture. Since the radial flow velocity decreases from the inner radius to the outer boundary, the values of Re is calculated using the maximum velocity at the inner radius as $\mathrm{V} = Q/(2\pi a \cdot \lambda)$.

5.4 Test Results

The steady-state radial flow is established by pumping constant water flow into the central cylindrical cavity. The required water flow rates may vary from 0.0001 ml/min to 50 ml/min depending on the level of axial loading. For each loading condition, three different flow rates

are applied to the sample in order to obtain an average estimation of fracture permeability. The time required to reach steady-state flow ranges between 1 min and 12 h depending on the fracture closure and flow rate. The flow rate controlled steady-state test becomes very time-consuming when axial load exceeds 3 MPa. The fracture closure has a significant effect on the permeability measurement. Pressure controlled test can therefore be utilized for measuring permeability of tight fracture.

Typical fracture permeability test results for S6-11 are shown in Figure 5.6. The normal stress-induced hysteretic behavior of a fracture is shown in Figure 5.7. The initial hydraulic aperture is recorded as λ_0=0.045 mm. The fracture shows significant closure during the normal loading cycles. At a peak load of 6 MPa during the second loading cycle, the hydraulic fracture aperture reduces to λ_{min}=0.001 mm (λ_{min}/λ_0=0.03), which means that the permeability has been reduced by three orders of magnitude (10^{-10} m^2 → 10^{-13} m^2). Upon complete unloading of the fracture, after two consecutive loading cycles, the residual hydraulic fracture aperture was estimated as λ_{res}=0.014 mm (λ_{res}/λ_0=0.30).

The loading process is terminated at an axial stress of 6 MPa, because further loading will lead to increase in permeability as a result of microfracture opening in the intact material. This can be clearly observed when some water percolate through those microcracks that are aligned along stratifications in the intact region. During the unloading process (6 MPa → 1 MPa), the fracture permeability decreases because of microcracks closure. Therefore, it is very important to ensure that the rock sample is perfectly intact before conducting fracture permeability test.

Selected fracture permeability test results for S6-16 under axial load of 1.0 MPa during first

unloading cycle are shown in Figure 5.8. Both flow rate controlled steady tests and pressure controlled steady tests provide similar estimation of permeability for the fracture. Sample S6-16 was subjected to three consecutive loading-unloading cycles with increasing peak stresses (10 MPa → 15 MPa → 20 MPa). The hysteretic behavior of a fracture under compression is shown in Figure 5.9. The initial fracture permeability without any compressive loading is measured to be 3.2×10^{-10} m^2 (λ_0=0.062 mm). At a peak load of 20 MPa during the third loading cycle, the fracture permeability is estimated as 3.2×10^{-14} m^2 (λ_{min}=0.0006 mm), which means that the permeability of a fracture has been reduced by four orders of magnitude under compressive stresses.

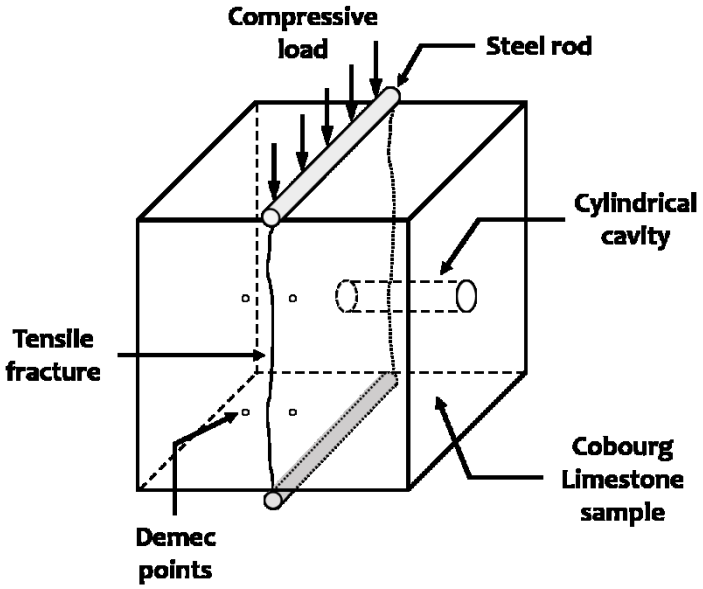

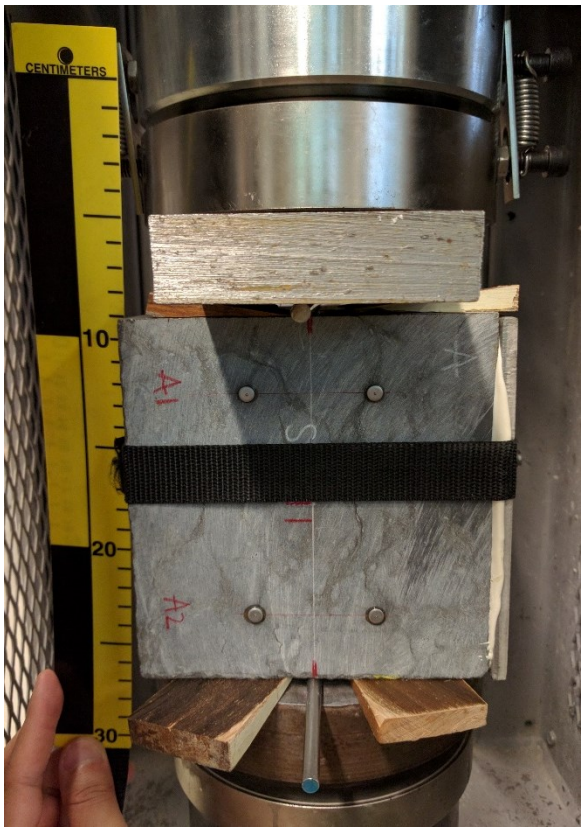

Figure 5.1 Introducing normal tensile fracture

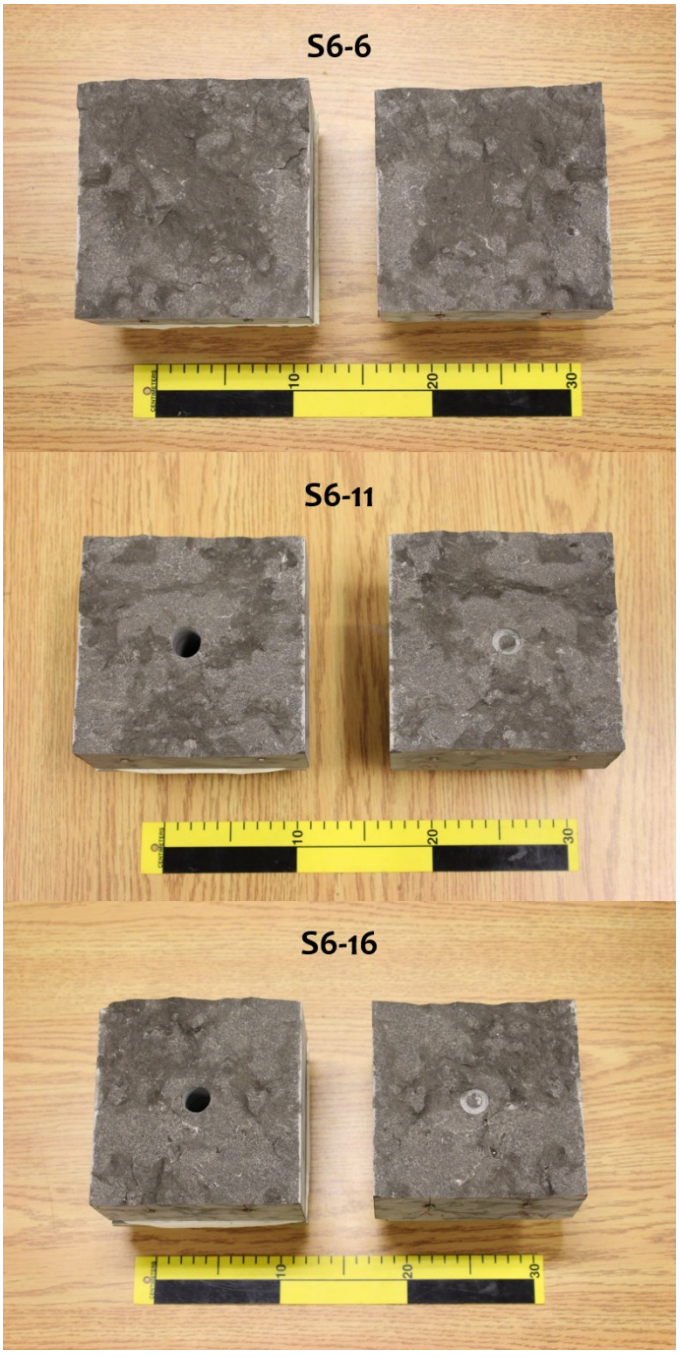

Figure 5.2 Photographs of fracture rough surface

S6-6

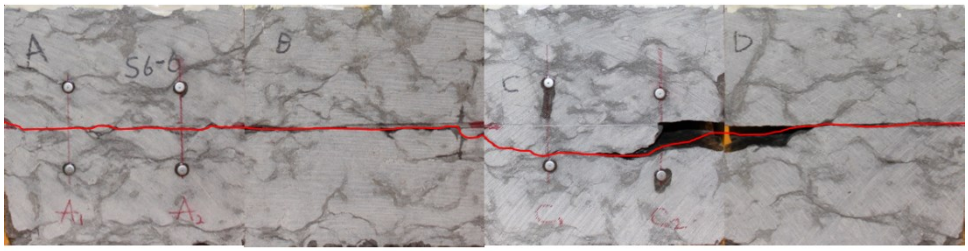

S6-11

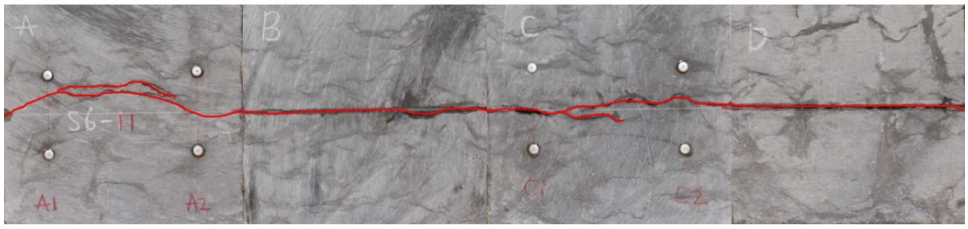

S6-16

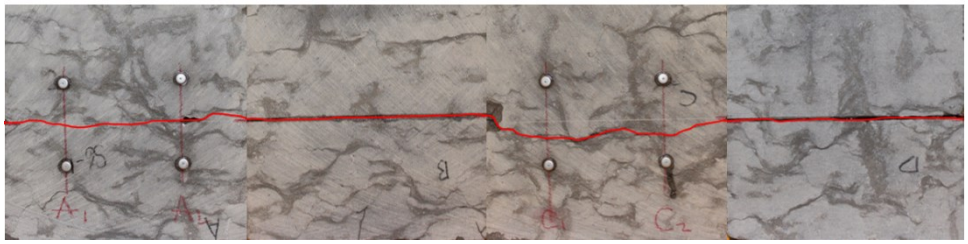

Figure 5.3 Fracture orientation

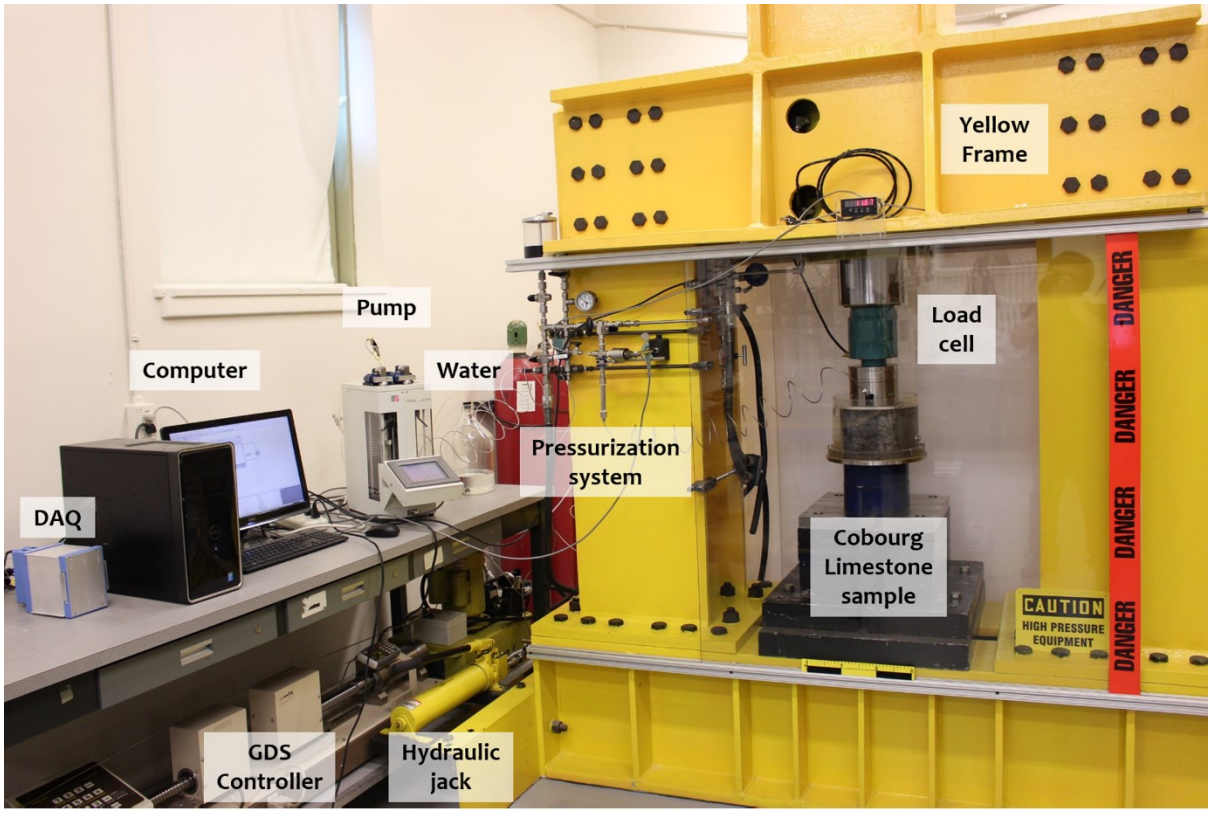

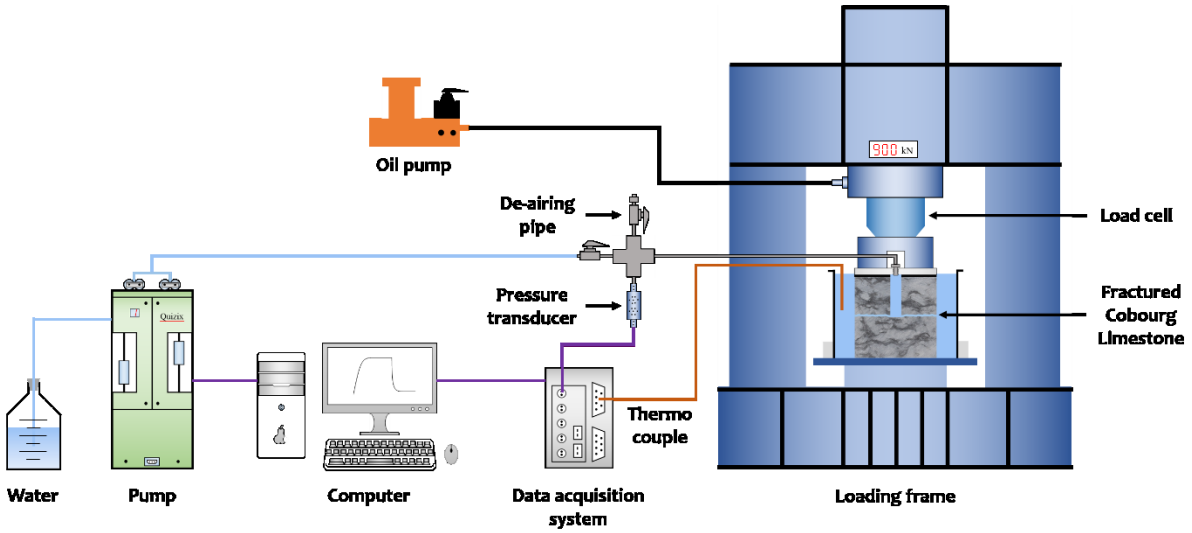

Figure 5.4 Experimental setup for fracture permeability test

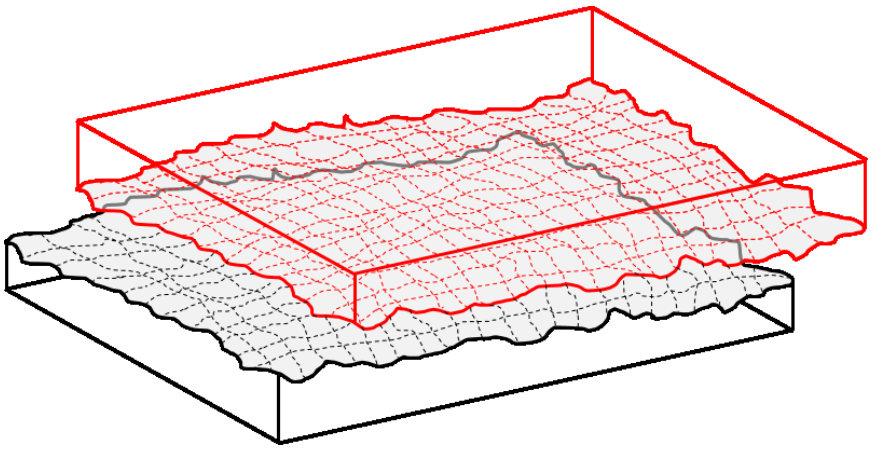

(a) Rough fracture

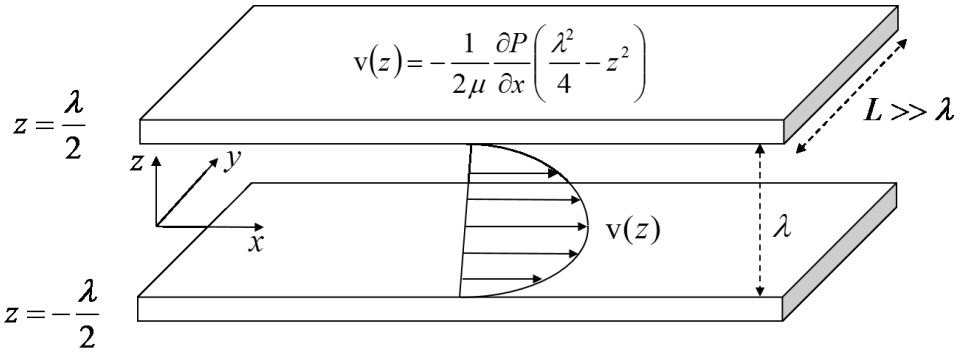

(b) Parallel plate model

Figure 5.5 Fluid flow in a fracture

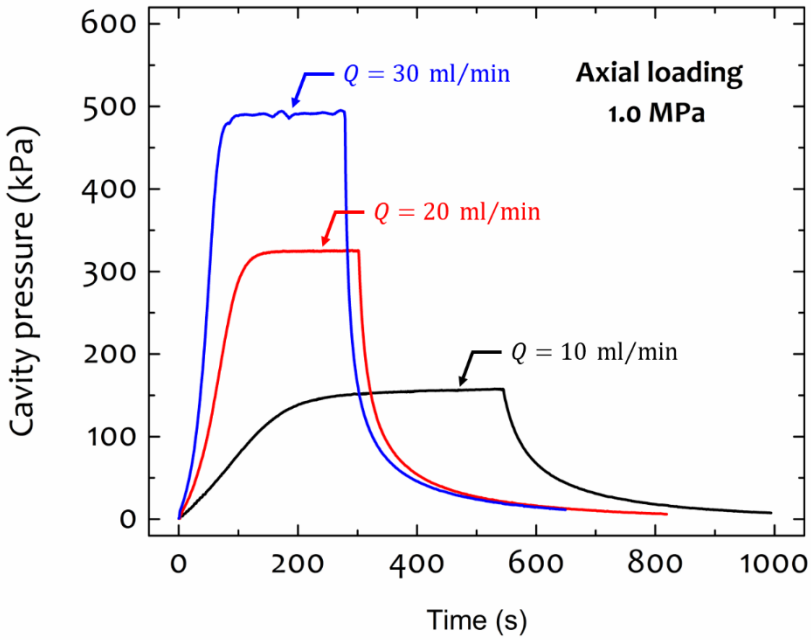

(a) 1.0 MPa during first loading cycle

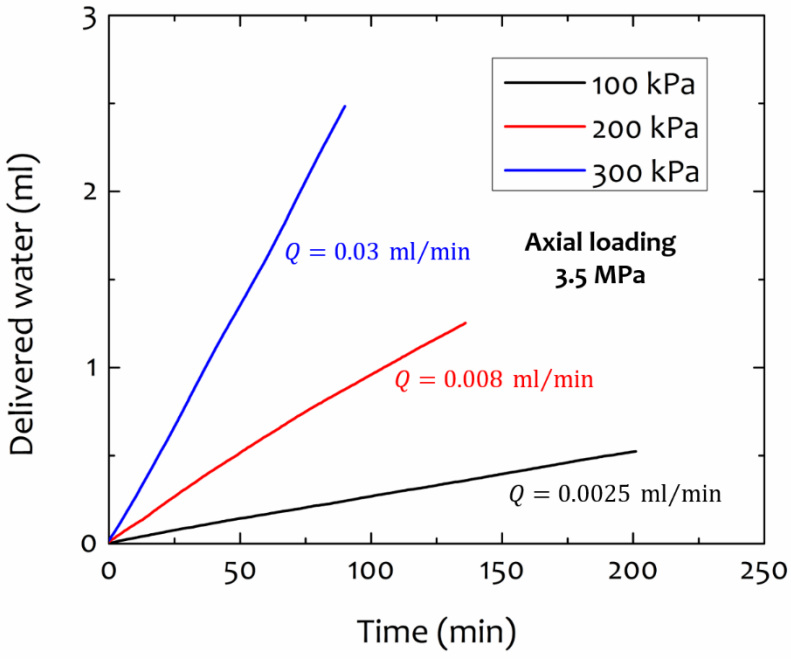

(b) 3.5 MPa during second unloading cycle

Figure 5.6 Fracture permeability test results for S6-11

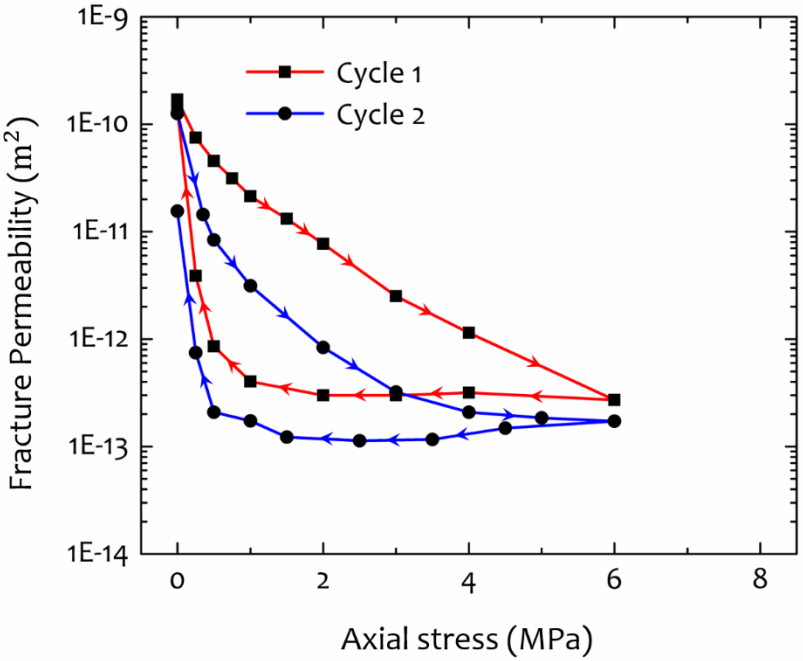

(a) Permeability

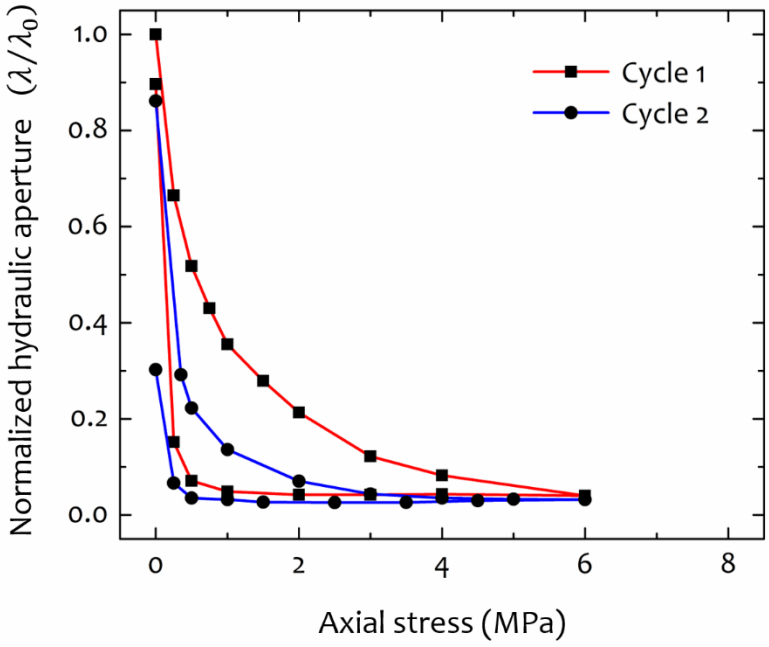

(b) Hydraulic aperture

Figure 5.7 Normal stress-induced hysteresis of a fracture for S6-11

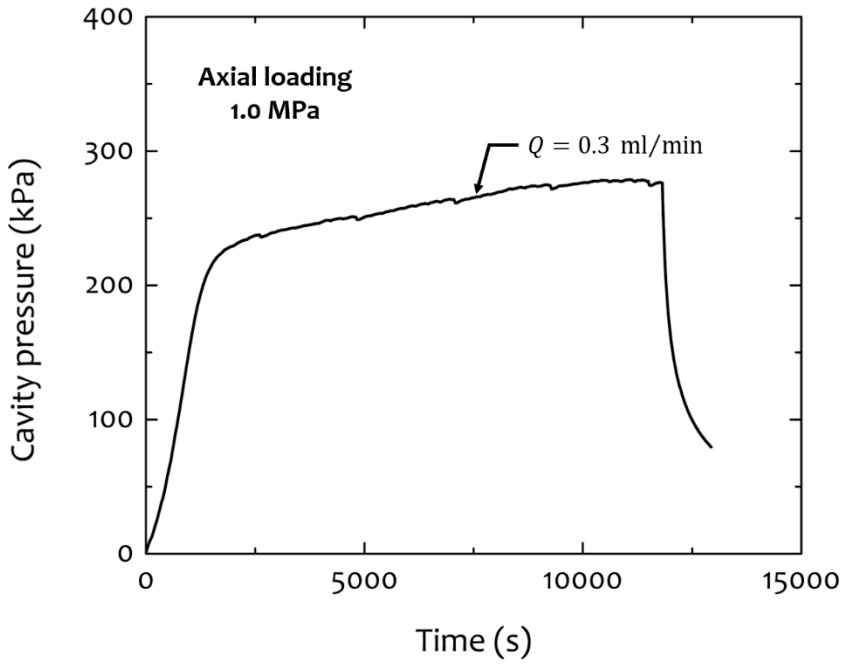

(a) Flow rate controlled test

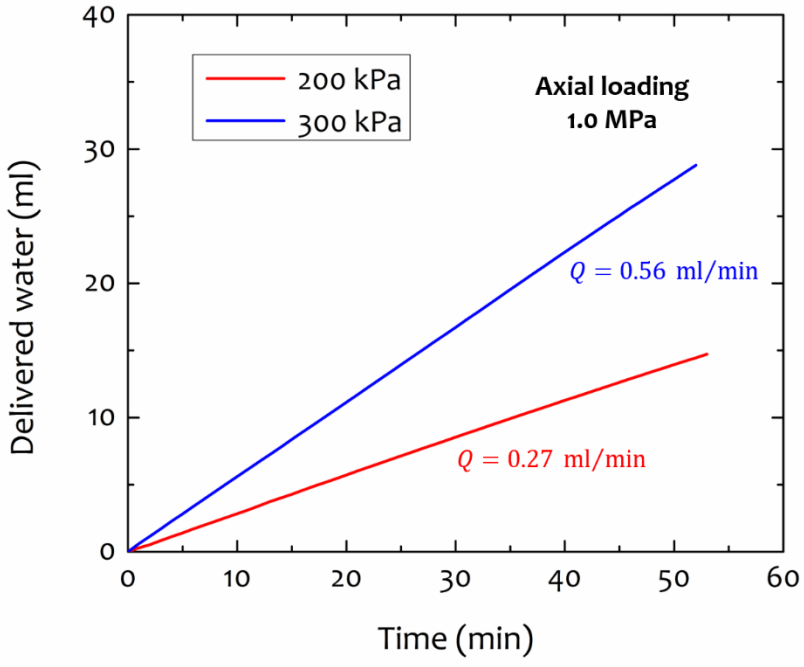

(b) Pressure controlled test

Figure 5.8 Fracture permeability test results for S6-16

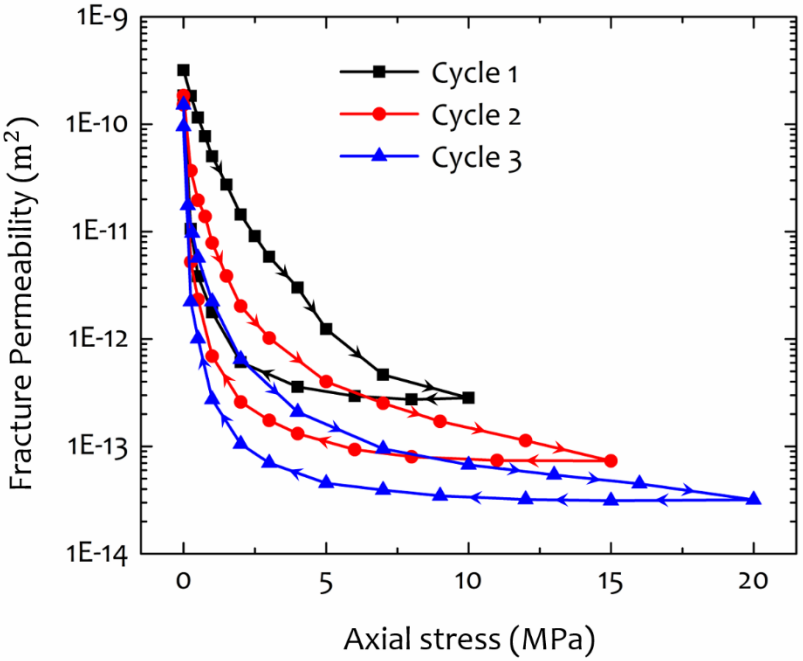

(a) Permeability

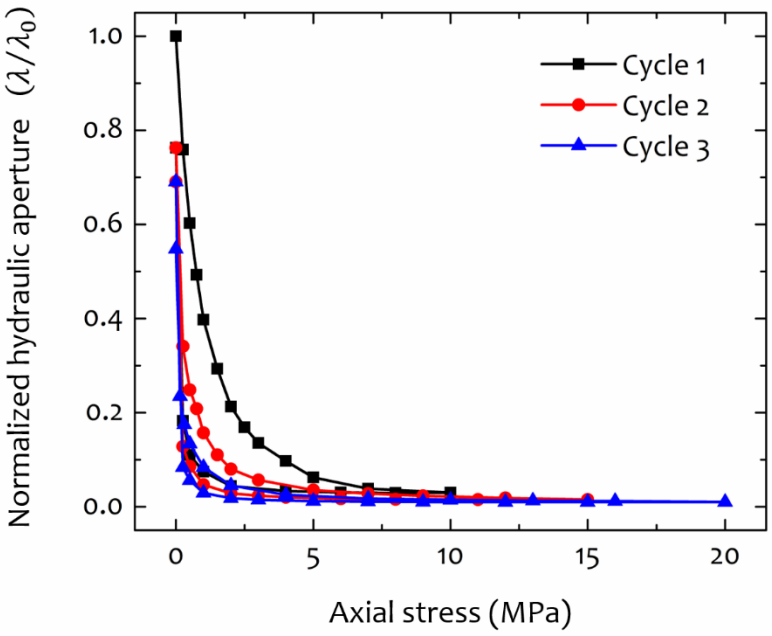

(b) Hydraulic aperture

Figure 5.9 Normal stress-induced hysteresis of a fracture for S6-16

Table 5.1 Fracture properties for cuboidal samples

Sample No.	Fracture aperture	Peak load	Tensile strength
S6-6	0.18 mm	75 kN	2.1 MPa
S6-11	0.19 mm	111 kN	3.0 MPa
S6-16	0.18 mm	97 kN	2.7 MPa

CHAPTER 6
CONCLUSIONS AND PROPOSAL FOR FUTURE WORK

6.1 Conclusions

In this research, the permeability characteristics of both intact and fractured Cobourg Limestone have been investigated by employing both transient and steady-state radial flow tests. Hydraulic pulse tests are used to measure the permeability of intact rock samples, which falls in the range of $[3, 39]\times10^{-21}$ m^2. The fracture permeability is estimated based on steady-state tests and reported to be between 10^{-14} and 10^{-10} m^2 under compressive stress $\sigma_n \in [0, 20]$ MPa. These experimental results indicate that the permeability of the intact rock is considerably lower than the fracture permeability and thus cracks in fractured geological media are responsible for most of the fluid flow.

Ideally, the best procedure for estimating the permeability of intact rocks is to perform steady-state tests. With low permeability, rocks such as the Cobourg Limestone, the attainment of steady state can be time consuming. Therefore, hydraulic pulse tests are the most convenient.

The discrepancy between the interpreted permeabilities for steady-state and transient tests could be explained by including the effects of trapped air in the pressurized cavity. The research completed in the Environmental Geomechanics Lab at McGill University has improved the interpretation of extremely low permeability of the intact geological materials such as the Cobourg Limestone.

Fracture permeability under normal stress exhibits hysteresis characteristics during loading-unloading cycles. Fracture permeability can be altered by four orders of magnitude under different levels of compressive stress. The hydro-mechanical properties of a single fracture determined from the experiments can be utilized for simulation of permeability evolution during the construction of Deep Geological Repository.

6.2 Proposal for Future Work

In this research, the experimental work performed on intact rock is limited to in-plane permeability estimation and the numerical interpretation assumes isotropic property for Cobourg Limestone. However, the material stratification shows clear anisotropic permeability characteristic. Therefore, more work is needed to measure permeability in both directions normal or parallel to the nominal bedding plane (K_h and K_v). A small-size cylindrical sample with either horizontal or vertical stratification may serve this purpose. Axial fluid flow can be applied in a conventional tri-axial cell with confining compression.

For the fracture permeability tests conducted in this study, the compressive stresses applied to

fractured cuboidal samples are limited to a maximum value of 20 MPa. The Obert-Hoek Cell can be used to apply high confining compression (up to 60 MPa) on cylindrical samples with 85 mm in diameter and 130 mm in length. A longitudinal tensile fracture will be generated using the Brazilian Splitting Test. The proposed fracture permeability test in Obert-Hoek Cell is schematically shown in Figure 6.1. Sealing is provided by a confining rubber membrane around the cylindrical surface. A steady-state rectilinear flow is established by pumping de-aired water at a constant flow rate into the fracture. Three cycles of compressive loads with increasing peak stress will be applied to the rock sample in order to study fracture permeability hysteresis.

Further study needs to extend the fracture flow tests to include large cuboidal samples of the Cobourg Limestone (350 mm) for investigation of possible scale effects. The loading frame in the McGill Environmental Geomechanics Laboratory is capable of applying compressive loading up to 7 MPa to such a cuboidal sample. A fracture surface roughness profile will be created by laser scanning the sample before and after normal loading tests in order to assess the asperity degradation during pure axial stressing. The contact area will also be measured using pressure sensitive films. These provide the input information for computational modelling of fluid flow through a heterogeneous fracture.

Future research could develop a computational framework to simulate the coupled thermo-hydro-mechanical processes involved in deep geological disposal of radioactive nuclear waste. The experimentally obtained stress-permeability properties of a single fracture are implemented into the constitutive model for rock joint to simulate block-scale permeability of

fractured porous media under variable stress states.

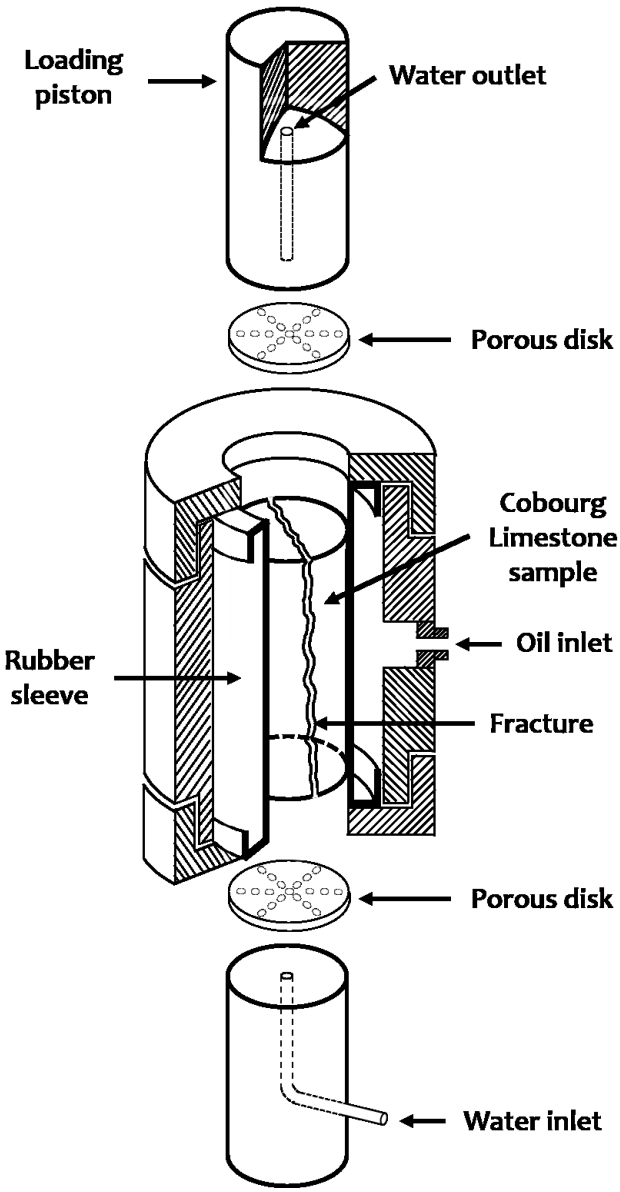

Figure 6.1 Obert-Hoek Cell fracture permeability test

REFERENCES

AECL (Atomic Energy Canada Limited). (1994). "Summary of the environmental impact statement on the concept for disposal of Canada's nuclear fuel waste." *AECL-10721, COG-93-11*.

Alonso, E.E., Alcoverro, J., Coste, F., et al. (2005). "The FEBEX benchmark test: case definition and comparison of modelling approaches." *International Journal of Rock Mechanics and Mining Sciences*, 42(5–6), 611 – 638.

Bandis, S.C., Lumsden, A.C., and Barton, N.R. (1983). "Fundamentals of rock joint deformation." *International Journal of Rock Mechanics and Mining Sciences and Geomechanics Abstracts*, 20(6), 249 – 268.

Barton, N., Bandis, S., and Bakhtar, K. (1985). "Strength, deformation and conductivity coupling of rock joints." *International Journal of Rock Mechanics and Mining Sciences and Geomechanics Abstracts*, 22(3), 121 – 140.

Bernabé, Y. (1986). "The effective pressure law for permeability in Chelmsford granite and Barre granite." *International Journal of Rock Mechanics and Mining Sciences and Geomechanics Abstracts*, 23(3), 267 – 275.

Bernaix, J. (1969). "New laboratory methods of studying the mechanical properties of rocks." *International Journal of Rock Mechanics and Mining Sciences*, 6(1), 43 – 90.

Bodvarsson, G.S., Boyle, W., Patterson, R., and Williams, D. (1999). "Overview of scientific investigations at Yucca Mountain – the potential repository for high-level nuclear waste." *Journal of Contaminant Hydrology*, 38(1–3), 3 – 24.

Boulon, M.J., Selvadurai, A.P.S., Benjelloun, H., and Feuga, B. (1993). "Influence of rock joint degradation on hydraulic conductivity." *International Journal of Rock Mechanics and Mining Sciences and Geomechanics Abstracts*, 30(7), 1311 – 1317.

Brace, W.F., Walsh, J.B., and Frangos, W.T. (1968). "Permeability of granite under high pressure." *Journal of Geophysical Research*, 73(6), 2225 – 2236.

Chen, Y., Hu, S., Wei, K., Hu, R., Zhou, C., and Jing, L. (2014). "Experimental characterization and micromechanical modelling of damage-induced permeability variation in Beishan granite." *International Journal of Rock Mechanics and Mining Sciences*, 71, 64 – 76.

Delay, J., Vinsot, A., Krieguer, J.M., Rebours, H., and Armand, G. (2007). "Making of the underground scientific experimental programme at the Meuse/Haute-0Marne underground research laboratory, North Eastern France." *Physics and Chemistry of the Earth, Parts A/B/C*, 32(1–7), 2 – 18.

Esaki, T., Du, S., Mitani, Y., Ikusada, K., and Jing, L. (1999). "Development of a shear-flow test apparatus and determination coupled properties for a single rock joint." *International Journal of Rock Mechanics and Mining Sciences*, 36(5), 641 – 650.

Escoffier, S., Homand, F., Giraud, A., Hoteit, N., and Su, K. (2005). "Under stress permeability determination of the Meuse/Haute-Marne mudstone." *Engineering Geology*, 81(3), 329 – 340.

Fredlund, D.G. (1976). "Density and compressibility characteristics of air-water mixtures." *Canadian Geotechnical Journal*, 13(4), 386 – 396.

Goodman, R.E. (1976). *Methods of geological engineering in discontinuous rocks*, West Publishing, New York.

Hans, J., and Boulon, M. (2003). "A new device for investigating the hydro-mechanical properties of rock joints." *International Journal for Numerical and Analytical Methods in Geomechanics*, 27(6), 513 – 548.

Hekimi, B. (2012). "The physical and mechanical properties of an argillaceous limestone." M.Eng. Thesis, McGill University, Montréal, QC, Canada.

Iwano, M. (1995). "Hydromechanical characteristics of a single rock joint." Ph.D. Thesis, Massachusetts Institute of Technology, Cambridge, MA, USA.

Jenner, L. (2011). "Radial hydraulic flow testing of an argillaceous limestone." M.Eng. Thesis, McGill University, Montréal, QC, Canada.

Jensen, M., Hobbs, M., Lam, T., Luhowy, D., McLay, J., Semec, B., and Vorauer, A. (2007). "Overview of Ontario power generation's proposed L&ILW deep geologic repository, Bruce Site, Tiverton, Ontario." *Proceedings of 60th Canadian Geotechnical Conference*,

Canadian Geotechnical Society, Ottawa, 620 – 627.

Jing, L., and Stephansson, O. (1995). "Mechanics of rock joints: Experimental aspects." *Mechanics of Geomaterial Interfaces*, A.P.S. Selvadurai, M.J. Boulon, eds., Elsevier, Amsterdam, 317 – 342.

Keller, C.K., and Kamp, G. (1992). "Slug tests with storage due to entrapped air." *Groundwater*, 30(1), 2 – 7.

Latham, J.P., Xiang, J.S., Belayneh, M., Nick, H.M., Tsang, C.F., and Blunt, M.J. (2013). "Modelling stress-dependent permeability in fractured rock including effects of propagating and bending fractures." *International Journal of Rock Mechanics and Mining Sciences*, 57, 100 – 112.

Lee, H.S., and Cho, T.F. (2002). "Hydraulic characteristics of rough fractures in linear flow under normal and shear load." *Rock Mechanics and Rock Engineering*, 35(4), 299 – 318.

Letendre, A. (2011). "Permeability changes in Lindsay Limestone due to isotropic compression." M.Eng. Thesis, McGill University, Montréal, QC, Canada.

Li, M., Yin, G., Xu, J., Cao, J., and Song, Z. (2016). "Permeability evolution of shale under anisotropic true triaxial stress conditions." *International Journal of Coal Geology*, 165, 142 – 148.

Min, K.B., Rutqvist, J., Tsang, C.F., and Jing, L. (2004). "Stress-dependent permeability of fractured rock masses: a numerical study." *International Journal of Rock Mechanics and Mining Sciences*, 41(7), 1191 – 1210.

Morrow, C.A., Shi, L.Q., and Byerlee, J.D. (1984). "Permeability of fault gouge under confining pressure and shear stress." *Journal of Geophysical Research*, 89(B5), 3193 – 3200.

Nasseri, M.H.B., Goodfellow, S.D., Lombos, L., and Young, R.P. (2014). "3-D transport and acoustic properties of Fontainebleau sandstone during true-triaxial deformation experiments." *International Journal of Rock Mechanics and Mining Sciences*, 69, 1 – 18.

Nemoto, K., Watanabe, N., and Tsuchiya, N. (2008). "Evaluation of fluid flow field in single rock fracture during frictional sliding." Water Dynamics: 5th International Workshop on Water Dynamics, 987(1), 123 – 128.

Neuzil, C.E., Cooley, C., Silliman, S.E., Bredehoeft, J.D., and Hsieh, P.A. (1981). "A transient laboratory method for determining the hydraulic properties of 'Tight' Rocks – II.

Application." *International Journal of Rock Mechanics and Mining Sciences and Geomechanics Abstracts*, 18(3), 253 – 258.

Nguyen, T.S., and Selvadurai, A.P.S. (1995). "Coupled thermal-mechanical-hydrological behavior of sparsely fractured rock: implications for nuclear fuel waste disposal." *International Journal of Rock Mechanics and Mining Sciences and Geomechanics Abstracts*, 32(5), 465 – 479.

Nguyen, T.S., and Selvadurai, A.P.S. (1998). "A model for coupled mechanical and hydraulic behavior of a rock joint." *International Journal for Numerical and Analytical Methods in Geomechanics*, 22(1), 29 – 48.

NWMO (Nuclear Waste Management Organization). (2011). "OPG's Deep Geologic Repository for low & intermediate level waste: Geosynthesis." *NWMO DGR-TR-2011-11*.

Olsson, W.A., and Brown, S.R. (1993). "Hydromechanical response of a fracture undergoing compression and shear." *International Journal of Rock Mechanics and Mining Sciences and Geomechanics Abstracts*, 30(7), 845 – 851.

Pan, Z., Ma, Y., Connell, L.D., Down, D.I., and Camilleri, M. (2015). "Measuring anisotropic permeability using a cubic shale sample in a triaxial cell." *Journal of Natural Gas Science and Engineering*, 26, 336 – 344.

Raven, K.G., and Gale, J.E. (1985). "Water flow in a natural rock fracture as a function of stress and sample size." *International Journal of Rock Mechanics and Mining Sciences & Geomechanics Abstract*, 22(4), 251 – 261.

Rutqvist, J., Wu, Y.S., Tsang, C.F., and Bodvarsson, G. (2002). "A modelling approach for analysis of coupled multiphase fluid flow, heat transfer, and deformation in fractured porous rock." *International Journal of Rock Mechanics and Mining Sciences*, 39(4), 429 – 442.

Rutqvist, J., and Stephansson, O. (2003). "The role of hydromechanical coupling in fractured rock engineering." *Hydrogeology Journal*, 11(1), 7 – 40.

Scherer, G.W. (2008). "Poromechanics analysis of a flow-through permeameter with entrapped air." *Cement and Concrete Research*, 38(3), 368 – 378.

Schuurman, I.E. (1966). "The compressibility of an air/water mixture and a theoretical relation between the air and water pressures." *Géotechnique*, 16(4): 269 – 281.

Selvadurai, A.P.S. (2015). "Normal stress-induced permeability hysteresis of a fracture in a

granite cylinder." *Geofluids*, 15(1-2), 37 – 47.

Selvadurai, A.P.S., and Carnaffan, P. (1997). "A transient pressure pulse method for the measurement of permeability of a cement grout." *Canadian Journal of Civil Engineering*, 24(3), 489 – 502.

Selvadurai, A.P.S., and Nguyen, T.S. (1997). "Scoping analysis of the coupled thermal-hydrological-mechanical behavior of the rock mass around a nuclear fuel waste repository." *Engineering Geology*, 47(4), 379 – 400.

Selvadurai, A.P.S., and Yu, Q. (2005). "Mechanics of a discontinuity in a geomaterial." *Computers and Geotechnics*, 32(2), 92 – 106.

Selvadurai, P.A., and Selvadurai, A.P.S. (2007). "On cavity flow permeability testing of a sandstone." *Groundwater*, 45(1), 93 – 97.

Selvadurai, A.P.S., and Selvadurai, P.A. (2010). "Surface permeability tests: experiments and modelling for estimating effective permeability." *Proceedings of the Royal Society of London A: Mathematical, Physical and Engineering Sciences*, 466(2122), 2819 – 2846.

Selvadurai, A.P.S., Letendre, A., and Hekimi, B. (2011). "Axial flow hydraulic pulse testing of an argillaceous limestone." *Environmental Earth Sciences*, 64(8), 2047 – 2058.

Selvadurai, A.P.S., and Jenner, L. (2013). "Radial flow permeability testing of an argillaceous limestone." *Groundwater*, 51(1), 100 – 107.

Selvadurai, A.P.S., and Najari, M. (2015). "Laboratory-scale hydraulic pulse testing: influence of air fraction in cavity on estimation of permeability." *Géotechnique*, 65(2), 126 – 134.

Selvadurai, A.P.S., and Najari, M. (2016). "Isothermal permeability of the argillaceous Cobourg Limestone." *Oil and Gas Science and Technology,* 71(4), 53.

Snow, D.T. (1965). "A parallel plate model of fractured permeable media." Ph.D. Thesis, University of California, Berkeley, CA, USA.

Souley, M., Homand, F., Pepa, S. and Hoxha, D. (2001). "Damage-induced permeability changes in granite: a case example at the URL in Canada." *International Journal of Rock Mechanics and Mining Sciences*, 38(2), 297 – 310.

Teufel, L. W. (1987). "Permeability changes during shear deformation of fractured rock." *Proceedings of the 28th US Symposium on Rock Mechanics*, Vol. 28, 473 – 480.

Thörn, J., Ericsson, L.O., and Fransson, Å. (2015). "Hydraulic and hydromechanical laboratory

testing of large crystalline rock cores." *Rock Mechanics and Rock Engineering*, 48(1), 61 – 73.

Watanabe, N., Hirano, N., and Tsuchiya, N. (2008). "Determination of aperture structure and fluid flow in a rock fracture by high-resolution numerical modelling on the basis of a flow-through experiment under confining pressure." *Water Resources Research*, 44(6), W06412.

White, F.W. (1986). *Fluid Mechanics*, 2nd ed., McGraw-Hill, Boston, MA.

Witherspoon, P.A., Amick, C.H., Gale, J.E., and Iwai, K. (1979). "Observations of a potential size effect in experimental determination of the hydraulic properties of fractures." *Water Resources Research*, 15(5), 1142 – 1146.

Xie, N., Yang, J.B., and Shao, J.F. (2014). "Study on the hydromechanical behavior of single fracture under normal stresses." *KSCE Journal of Civil Engineering*, 18(6), 1641 – 1649.

Yeo, I.W., De Freitas, M.H., and Zimmerman, R.W. (1998). "Effect of shear displacement on the aperture and permeability of a rock fracture." *International Journal of Rock Mechanics and Mining Sciences*, 35(8), 1051 – 1070.

Zhou, C.B., Sharma, R.S., Chen, Y.F., and Rong, G. (2008). "Flow-stress coupled permeability tensor for fractured rock masses." *International Journal for Numerical and Analytical Methods in Geomechanics*, 32(11), 1289 – 1309.

Zimmerman, R.W., and Yeo, I.W. (2000). "Fluid flow in rock fractures: From the Navier-Stokes equations to the cubic law." *Dynamics of Fluids in Fractured Rock*, B. Faybishenko, P.A. Witherspoon, S.M. Benson, eds., American Geophysical Union, Washington, DC, 213 – 224.